A study of the Arctic NO_y budget above Eureka, Canada

R. Lindenmaier,[1] K. Strong,[1] R. L. Batchelor,[2] P. F. Bernath,[3] S. Chabrillat,[4] M. P. Chipperfield,[5] W. H. Daffer,[6] J. R. Drummond,[7] W. Feng,[5] A. I. Jonsson,[1] F. Kolonjari,[1] G. L. Manney,[6,8] C. McLinden,[9] R. Ménard,[10] and K. A. Walker[1]

Received 4 May 2011; revised 27 September 2011; accepted 29 September 2011; published 8 December 2011.

[1] Four years of trace gas measurements have been acquired using the Bruker 125HR Fourier Transform Infrared (FTIR) spectrometer installed at the Polar Environment Atmospheric Research Laboratory (PEARL) in the Canadian high Arctic. These have been compared with data from three models, namely the Canadian Middle Atmosphere Model Data Assimilation System (CMAM-DAS), the Global Environmental Multiscale stratospheric model with the online Belgium Atmospheric CHemistry package (GEM-BACH), and the off-line 3D chemical transport model SLIMCAT to assess the total reactive nitrogen, NO_y, budget above Eureka, Nunavut (80.05°N, 86.42°W). The FTIR data have been also compared with satellite measurements by the Atmospheric Chemistry Experiment-Fourier Transform Spectrometer (ACE-FTS). The FTIR is able to measure four of the five primary species that form NO_y: NO, NO_2, HNO_3, and $ClONO_2$, while the fifth, N_2O_5, was obtained using the $N_2O_5/(NO + NO_2)$ ratio derived from the models and ACE-FTS. Combining these results, a four-year time series of NO_y 15–40 km partial columns was calculated. Comparisons with each model were made, revealing mean differences (± standard error of the mean) relative to the FTIR of (−16.0 ± 0.6)%, (5.5 ± 1.0)%, and (−5.8 ± 0.4)% for CMAM-DAS, GEM-BACH, and SLIMCAT, respectively. The mean difference between the ACE-FTS and FTIR NO_y partial columns was (5.6 ± 2.3)%. While we found no significant seasonal and interannual differences in the FTIR NO_y stratospheric columns, the partial columns display nearly twice as much variability during the spring compared to the summer period.

Citation: Lindenmaier, R., et al. (2011), A study of the Arctic NO_y budget above Eureka, Canada, *J. Geophys. Res.*, *116*, D23302, doi:10.1029/2011JD016207.

1. Introduction

[2] Reactive nitrogen species play an important role in the chemistry of the stratosphere. Nitrogen oxides (NO_x = NO + NO_2) are responsible for significant ozone destruction in the middle stratosphere and furthermore influence the partitioning of the hydrogen, chlorine, and bromine species in the lower stratosphere, thereby affecting ozone loss rates also in this region. Total reactive nitrogen (NO_y) is defined as

$$NO_y = NO + NO_2 + NO_3 + HNO_3 + 2 \times N_2O_5 + ClONO_2 + BrONO_2 + HO_2NO_2. \quad (1)$$

Approximately 97% of the NO_y budget can be accounted for by NO, NO_2, HNO_3, $ClONO_2$, and N_2O_5 [*Brohede et al.*, 2008]. Figure 1 shows the contribution of these five species to the NO_y budget at Eureka as simulated by SLIMCAT for various seasons. The noon profiles were averaged by season from August 2006 to March 2010, (a) November–December–January (NDJ) corresponding to polar night (Figure 1a), February–March–April (FMA) corresponding to polar sunrise (days of varying length from completely dark to completely light) (Figure 1b), May–June–July (MJJ) corresponding to 24 h sunlight (Figure 1c), and August–September–October (ASO) corresponding to polar sunset (as per FMA, reversed) (Figure 1d). Throughout the rest of

[1]Department of Physics, University of Toronto, Toronto, Ontario, Canada.
[2]Atmospheric Chemistry Division, National Center for Atmospheric Research, Boulder, Colorado, USA.
[3]Department of Chemistry, University of York, York, UK.
[4]Chemical Weather Services, Belgian Institute for Space Aeronomy, Brussels, Belgium.
[5]Institute for Climate and Atmospheric Science, School of Earth and Environment, University of Leeds, Leeds, UK.
[6]Jet Propulsion Laboratory, Pasadena, California, USA.
[7]Department of Physics and Atmospheric Science, Dalhousie University, Halifax, Nova Scotia, Canada.
[8]Department of Physics, New Mexico Institute of Mining and Technology, Soccoro, New Mexico, USA.
[9]Air Quality Research Division, Environment Canada, Downsview, Ontario, Canada.
[10]Air Quality Research Division, Environment Canada, Dorval, Quebec, Canada.

Copyright 2011 by the American Geophysical Union.
0148-0227/11/2011JD016207

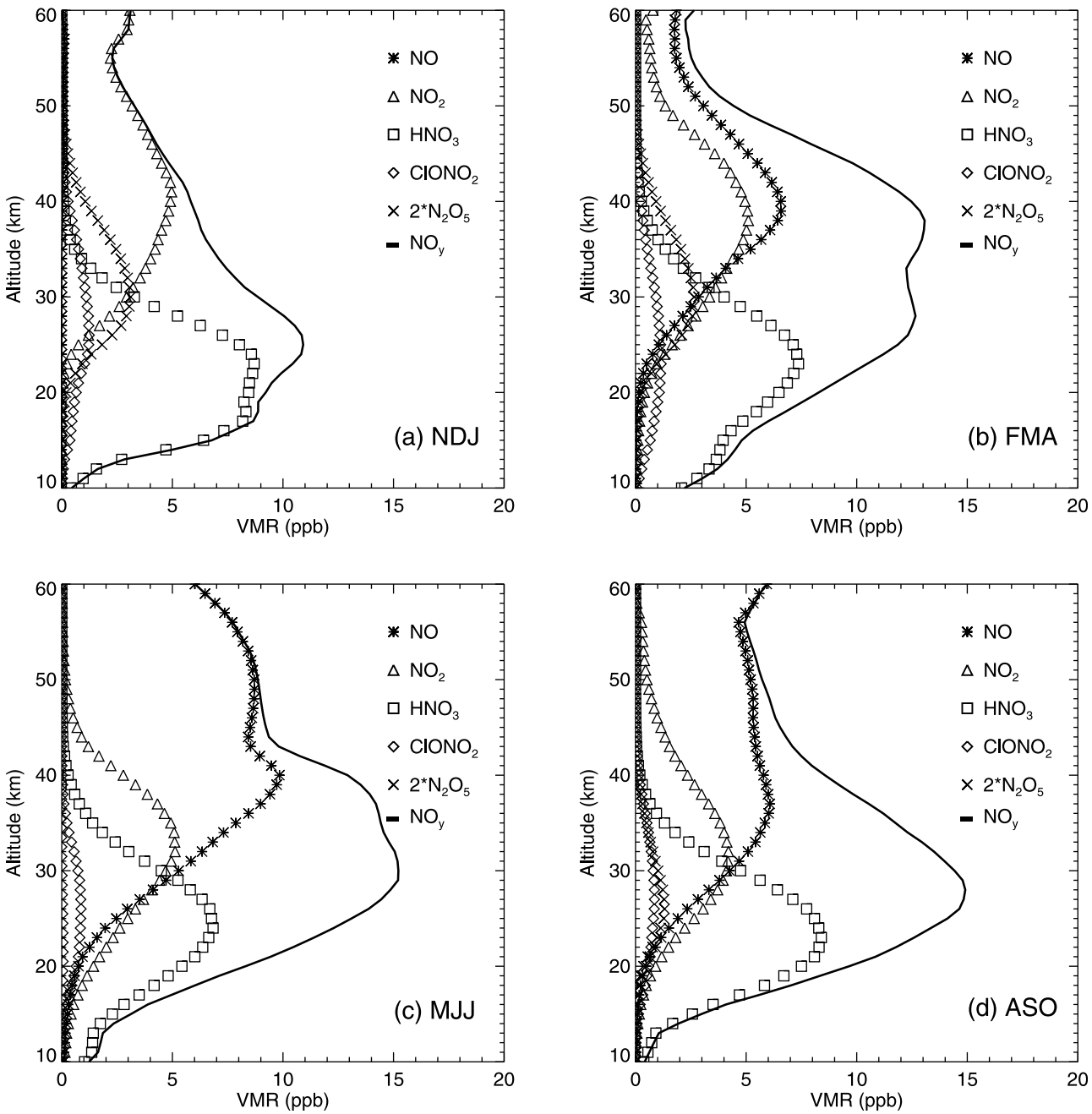

Figure 1. Contribution of the five primary reactive nitrogen species to the NO_y budget at Eureka as simulated by SLIMCAT. The noon profiles are averaged by season from August 2006 to March 2010: (a) November–December–January (NDJ) corresponding to polar night, (b) February–March–April (FMA) corresponding to polar sunrise (days of varying length from completely dark to completely light), (c) May–June–July (MJJ) corresponding to 24 h sunlight, and (d) August–September–October (ASO) corresponding to polar sunset (as per FMA, reversed).

this paper, we refer to the sum of these five nitrogen species as 5-NO_y.

[3] The main source of stratospheric NO_y is oxidation of N_2O, which produces NO. NO is rapidly oxidized to NO_2 by reaction with O_3. NO_2, in turn, is subject to photolysis, regenerating NO. In the upper stratosphere (~40 km), where the timescale of exchange between NO and NO_2 is less than 100 s, a quasi-steady state is quickly established. NO and NO_2 have strong diurnal variability. As the sun sets, NO concentrations decrease, while the NO_2 concentrations increase. At sunrise, the process is reversed. This behavior is well described by photochemical box models [e.g., *McLinden et al.*, 2000; *Brohede et al.*, 2007]. A smaller and sporadic source of NO_y is the precipitation of energetic particles that form NO in the mesosphere and lower thermosphere, which can be transported downward into the polar stratosphere [e. g., *Randall et al.*, 2005, 2007, 2009].

This contribution constitutes approximately 2% of the total global budget of NO_y, but can be higher in the polar regions.

[4] The sinks of stratospheric NO_y include transport into the troposphere and photolysis in the upper stratosphere (usually above 40 km). During the polar night and early spring, HNO_3 may be removed from the gas phase and trapped in polar stratospheric clouds (PSCs) through heterogeneous reactions. If these particles grow sufficiently large, they undergo sedimentation, resulting in NO_y being removed from the stratosphere by the process of denitrification [*Fahey et al.*, 1989; *Jin et al.*, 2006; *Santee et al.*, 2008]. Evaporation of these particles at lower altitudes can release HNO_3, renitrifying the lower atmosphere [*Dibb et al.*, 2006; *Grossel et al.*, 2010].

[5] Recent studies have shown that N_2O is increasing at a rate of 2.6% per decade [*Forster et al.*, 2007] and it has been described as the most important anthropogenic ozone-depleting substance emitted today [*Ravishankara et al.*, 2009]. On the other hand, the stratospheric effects of climate change are predicted to reduce the NO_y/N_2O ratio [*Plummer et al.*, 2010], so the future evolution of NO_y is unclear. This makes measurements of long-term changes in NO_y of particular scientific interest.

[6] Efforts have been made to measure NO_y from space since 1978, when the Limb Infrared Monitor of the Stratosphere (LIMS) satellite instrument was launched onboard Nimbus-7 and measured HNO_3 and NO_2 [*Gille and Russell*, 1984]. Later, NO and NO_2 measurements made by the Halogen Occultation Experiment (HALOE) were combined with HNO_3 and $ClONO_2$ measurements made by the Cryogenic Limb Array Etalon Spectrometer (CLAES) to determine NO_y for 1992–1994 [*Danilin et al.*, 1999]. The Michelson Interferometer for Passive Atmospheric Sounding (MIPAS), launched in 2002 onboard the European Environmental Satellite (ENVISAT), was the first satellite instrument to measure all five primary NO_y species [*Mengistu Tsidu et al.*, 2005]. In 2003, the Atmospheric Chemistry Experiment Fourier Transform Spectrometer (ACE-FTS) onboard SCISAT was launched [*Bernath et al.*, 2005]. It remains operational and measures the five primary NO_y species and HNO_4, from which a global NO_y climatology has recently been derived [*Jones et al.*, 2011].

[7] Stratospheric reactive nitrogen has been also measured by other techniques using balloon-borne instruments [e.g., *Ridley et al.*, 1984; *Kondo et al.*, 1994] and in situ lower stratospheric aircraft sampling [e.g., *Kawa et al.*, 1992]. During the spring and summer of 1997, a coordinated campaign of balloon, aircraft, and ground-based measurements of the atmospheric composition was conducted from Fairbanks, Alaska (65°N, 148°W), to gain a more direct and quantitative understanding of the reasons for seasonal ozone loss observed during the high-latitude summer [*Toon et al.*, 1999]. As part of the Photochemistry of Ozone Loss in the Arctic Region in Summer (POLARIS) campaign, the Jet Propulsion Laboratory (JPL) performed two balloon flights of the MkIV interferometer from Fairbanks and also performed ground-based Fourier Transform Infrared (FTIR) column observations. These captured the temporal evolution of the column abundances of the NO_x to NO_y ratio, and were compared with similar ground-based measurements performed at Ny Ålesund, Spitzbergen (79°N, 12°E). NO_y was obtained by summing the individual column abundances of NO + NO_2 + HNO_3 + $ClONO_2$, without considering N_2O_5. FTIR measurements of individual NO_y primary species have been made at other polar stations: Kiruna, Harestua, Ny Ålesund, and Esrange [*Mellqvist et al.*, 2002], Kiruna [*Griesfeller et al.*, 2006], Eureka and Thule [*Farahani et al.*, 2007], and Arrival Heights [*Wood et al.*, 2004].

[8] The goals of this work are to derive an NO_y partial column data product from ground-based FTIR measurements at Eureka in the Canadian high Arctic, to use the resulting four-year time series to assess seasonal and interannual variability, and to compare the results with three atmospheric models and satellite data.

[9] This paper is organized as follows: Section 2 introduces the measurement site and the ground-based and satellite instruments. Section 3 describes the three atmospheric models. Section 4 presents the comparison of the model and FTIR results. Section 5 presents the comparison of the ACE-FTS and the FTIR data for four Canadian Arctic ACE Validation Campaigns conducted during the springs of 2007, 2008, 2009, and 2010. Section 6 discusses the seasonal and interannual variability of NO_y seen in the FTIR measurements, and section 7 summarizes the results.

2. Instruments

2.1. CANDAC Bruker IFS 125HR

[10] The Polar Environment Atmospheric Research Laboratory (PEARL) was established in 2005 by the Canadian Network for the Detection of Atmospheric Change (CANDAC). It is located on Ellesmere Island at Eureka, Nunavut (80.05°N, 86.42°W), 610 m above sea level. The Bruker 125HR FTIR spectrometer (henceforth, the FTIR) was installed in July 2006 and is a high-resolution spectrometer that records solar absorption spectra throughout the sunlit part of the year (mid-February to mid-October). As a comprehensive description of the instrument is given by *Batchelor et al.* [2009], we mention here only its main characteristics. The FTIR uses a sequence of seven narrow-band interference filters covering the mid-infrared spectral range (600–4300 cm^{-1}), while measuring with either an InSb or an HgCdTe detector with a KBr beamsplitter. The solar absorption measurements consist of two or four co-added interferograms recorded in both the forward and backward directions at a resolution of 0.0035 cm^{-1} (the maximum optical path difference is 257 cm), which are then Fourier transformed to yield the spectrum. No apodization is applied to the interferograms.

[11] The altitude-dependent volume mixing ratio (VMR) profiles were retrieved from the spectra using SFIT2 [*Pougatchev et al.*, 1995], a profile retrieval algorithm that employs the Optimal Estimation Method (OEM) developed by *Rodgers* [2000]. The OEM is a regularization method that retrieves VMR profiles from a statistical weighting of the a priori information and the measurements. The averaging kernel matrix produced during the iterative process can be used to characterize the information content of the retrievals. The VMR profiles are converted to density profiles using temperature and pressure profiles and integrated throughout the column to yield the column densities. Partial column densities of NO, NO_2, HNO_3, and $ClONO_2$ for the 15–40 km range were derived. This altitude range was chosen based on the averaging kernels (the rows of the averaging kernel

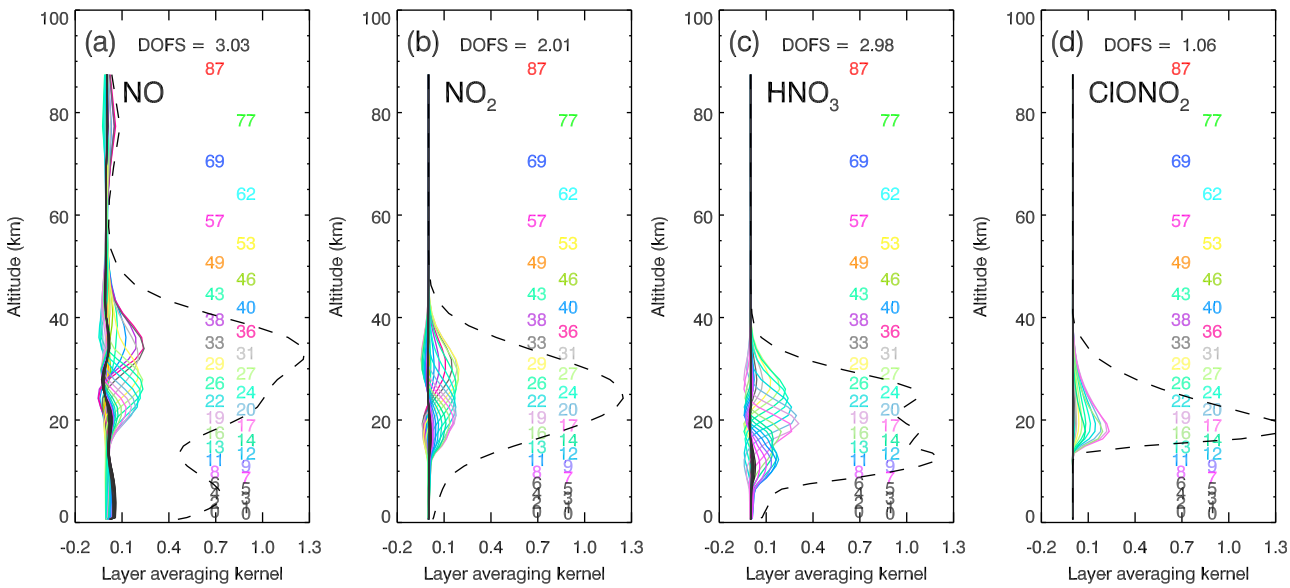

Figure 2. Typical FTIR layer averaging kernels for 6 March 2009 for (a) NO, (b) NO_2, (c) HNO_3, and (d) $ClONO_2$. The dashed line represents the sensitivity; i.e., the fraction of information coming from the measurement rather than from the a priori. The numbers on the right indicate the altitude of each averaging kernel. The degrees of freedom for signal (DOFS), defined as the trace of the averaging kernel matrix, are also included.

matrix) and the sensitivity (the sum of the elements of the averaging kernels) for each of these four species [*Vigouroux et al.*, 2008]. The latter indicates the fraction of the retrieval at each altitude that comes from the measurement rather than the a priori. Figure 2 shows an example of layer averaging kernels for spectra acquired on 6 March 2009. The dashed line shows the sensitivity for each case, being mostly above 50% for the 15–40 km altitude range. The degrees of freedom for signal (DOFS), defined as the trace of the averaging kernel matrix, are also shown. Figure 3 shows the 15–40 km partial column averaging kernels (red dashed lines), and for comparison, the 0.61–100 km total column averaging kernels (black continuous lines) for the same spectra.

[12] SFIT2 v.3.92c and the HITRAN 2004+ updates line list [*Rothman et al.*, 2005] were used for the retrievals. The VMR a priori profiles were derived from a variety of climatological data sets. For NO and NO_2, more than 7000 HALOE profiles from 1991 to 2005 were used [*Gordley et al.*, 1996] (http://haloedata.larc.nasa.gov/home/index.php). Monthly mean VMRs reported in the SPARC2000

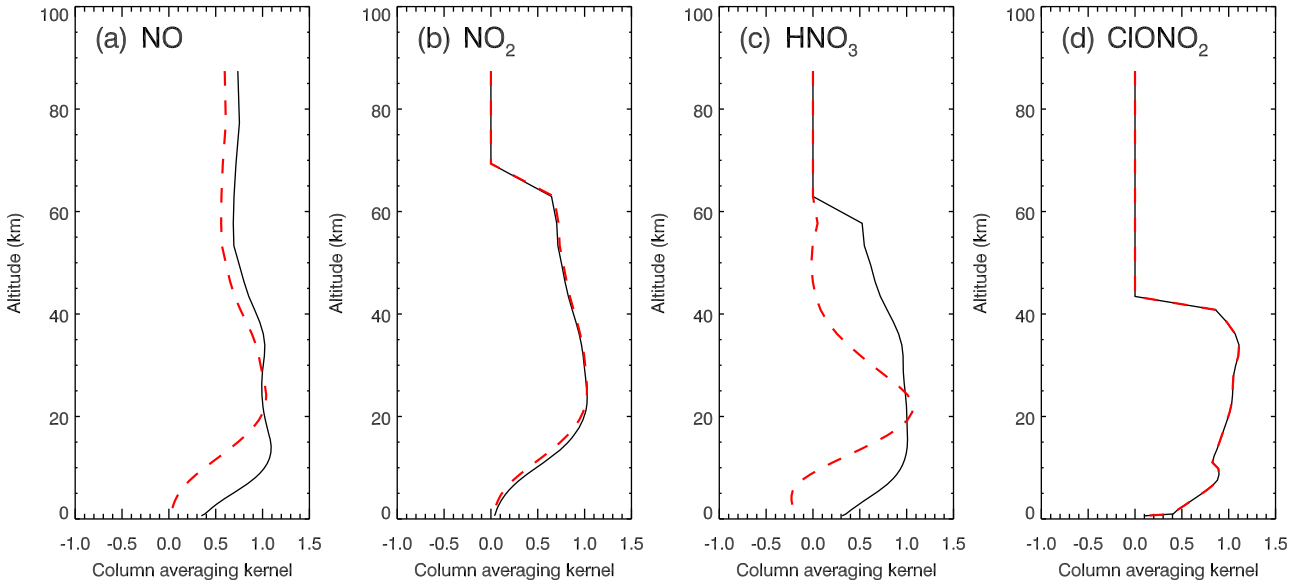

Figure 3. Typical FTIR column averaging kernels for 6 March 2009 for (a) NO, (b) NO_2, (c) HNO_3, and (d) $ClONO_2$. The red dashed line represents the 15–40 km partial column averaging kernels. The black line corresponds to the total column averaging kernel.

Table 1. Summary of Retrieval Microwindows (or Multimicrowindows), Interfering Species, $\mathbf{S_a}$, Interlayer Correlation (ILC) Parameter, Degrees of Freedom for Signal (DOFS), and Estimated Total Errors for the Four NO_y Species Retrieved From the FTIR Spectra[a]

Gas	Microwindow(s) (cm^{-1})	Interfering Species	S_a (%)	ILC (km)	DOFS	Total Measurement Error (%)
NO	1875.645–1875.840	H_2O	50	4	2.3	6.9
	1899.850–1900.150	N_2O, CO_2, H_2O				
	1900.450–1900.550	CO_2, H_2O				
	1903.070–1903.180	CO_2, H_2O				
	1906.100–1906.200	CO_2, H_2O, N_2O				
NO_2	2914.590–2914.707	CH_4, CH_3D	50	4	1.85	14.5
	2918.100–2918.350	CH_4, CH_3D				
	2919.400–2919.650	CH_4, CH_3D, H_2O				
	2922.360–2922.750	CH_4, H_2O, HDO				
	2924.750–2924.925	CH_4, H_2O, HDO, OCS				
HNO_3	867.500–870.000	H_2O, OCS, NH_3	50	4	2.1	13.3
$ClONO_2$	779.850–780.45	O_3 (P), CO_2 (P), HNO_3	100	4	0.8	22.5[b]
	782.550–782.870	O_3 (P), CO_2 (P), H_2O, HNO_3				
	938.300–939.300	CO_2 (P)				

[a]The multimicrowindows are fitted simultaneously. Interfering species are usually scale fitted, profile fitting being indicated by (P). DOFS were calculated as the trace of **A,** the averaging kernel matrix, and a mean value is given below for the entire measurement interval. The total error was calculated as described by *Batchelor et al.* [2009], with individual errors resulting from measurement, model parameter, and interference errors added in quadrature. A mean total error is shown for the February–October period.

[b]In the case of $ClONO_2$ total errors are much lower during the sunrise period, ~4%, and higher during summer, ~50%.

compilations were used for HNO_3 [*Randel et al.*, 2002] (http://www.sparc.sunysb.edu/html/updates.html), while MIPAS VMR profiles from 2002 to 2004 were used for $ClONO_2$ [*Höpfner et al.*, 2007]. For each species, the a priori profiles were taken to be the zonally averaged mean VMR profiles of the climatological data sets available at latitudes higher than 65°N. The mean profiles were calculated taking into account the nonuniform temporal distribution of input profiles, to eliminate sampling biases.

[13] The same data sets were used to calculate VMR variances as a function of altitude. From these, the largest values were adopted as the diagonal elements of the a priori $\mathbf{S_a}$ covariance matrix to ensure that $\mathbf{S_a}$ encompassed the full range of observed variability. For $ClONO_2$, whose VMR profile experiences substantial seasonal variations (by a factor of two or greater), a variance of 100% was used for the diagonal elements of $\mathbf{S_a}$. An interlayer correlation (ILC) parameter was also determined from correlation matrices calculated using the same climatological data sets and was used to generate the off-diagonal elements of $\mathbf{S_a}$ based on a Gaussian distribution. See Table 1 for the diagonal values of $\mathbf{S_a}$ and the ILC.

[14] The ad hoc signal-to-noise ratios (SNRs) used for determining the measurement covariances were selected for each gas using the trade-off curve method described by *Batchelor et al.* [2009]. Daily pressure-temperature profiles were obtained from the average of the twice-daily radiosondes launched at Eureka, supplemented with the National Centre for Environmental Prediction (NCEP) profiles above the maximum altitudes of the radiosondes, and with the 1976 U.S. standard atmosphere profile above 50 km. A summary of the spectral fitting microwindows that have been used for each gas, the fitted interfering species, the DOFS, and an estimated error in the partial column is given in Table 1.

[15] The error calculations in this work are based on the methodology of *Rodgers* [1976, 1990]. In addition to the smoothing ($\mathbf{S_s}$) and measurement ($\mathbf{S_m}$) errors, forward model parameter errors have been calculated as described by *Rodgers* [2000] using a perturbation method and our best estimate of the uncertainties in temperature ($\mathbf{S_{temp}}$), line intensity ($\mathbf{S_{lint}}$), air-broadened half width ($\mathbf{S_{lwdth}}$), and solar zenith angle ($\mathbf{S_{sza}}$). The uncertainty used for the temperature error calculation was in the range 2 to 9 K, depending on the altitude. For the SZA an uncertainty of 0.125° was used, while for the line parameters the uncertainty was determined from the maximum uncertainty within the range quoted in the HITRAN 2004 linelist. Interference errors, as described by *Rodgers and Connor* [2003] have been calculated to account for uncertainties in retrieval parameters (i.e., wavelength shift, instrument line shape, background slope and curvature, and phase error) and in interfering gases simultaneously retrieved. These interference errors are referred to as $\mathbf{S_{int1}}$ and $\mathbf{S_{int2}}$, respectively. The error budget calculation is described in depth by *Batchelor et al.* [2009].

[16] The total measurement error ($\mathbf{S_{TOTAL}}$) has been determined by adding all components in quadrature and not taking into account differences between the random and systematic components:

$$\mathbf{S_{TOTAL}} = \left\{\left(\mathbf{S_m^2} + \mathbf{S_{temp}^2} + \mathbf{S_{int1}^2} + \mathbf{S_{int2}^2} + \mathbf{S_{sza}^2}\right) + \mathbf{S_{lint}^2} + \mathbf{S_{lwdth}^2} + \mathbf{S_s^2}\right\}^{1/2}. \quad (2)$$

[17] In this study, the smoothing error was excluded from this total as this was accounted for when the comparison profiles were smoothed by the FTIR averaging kernels (as described in section 4.1). The total measurement error shown in Table 1 was calculated excluding the smoothing error.

2.2. ACE-FTS

[18] The Atmospheric Chemistry Experiment (or SCISAT) Canadian satellite mission was launched in August 2003 and orbits the Earth in a 74° inclined circular orbit at an altitude of 650 km [*Bernath et al.*, 2005]. Working in solar occultation, the ACE instruments provide profile information from 85°N to 85°S for temperature, pressure, and more than 30 different atmospheric species. The satellite has overpasses above Eureka during polar sunrise (February–March), when

ozone depletion chemistry can be observed, and again near polar sunset in September–October.

[19] The primary ACE instrument is a high resolution (0.02 cm^{-1}) Fourier transform spectrometer (henceforth the ACE-FTS), that has a similar spectral range to the FTIR, from 750 to 4400 cm^{-1}, but a considerably higher vertical resolution due to the limb-sounding geometry [*Bernath et al.*, 2005]. Pressure and temperature profiles are determined from the ACE-FTS spectra (based on a detailed CO_2 analysis) and further used to retrieve trace gas volume mixing ratio profiles with a nonlinear least squares fitting algorithm described by *Boone et al.* [2005]. The data set used for this comparison is v2.2 with updates for N_2O_5.

3. Models

3.1. CMAM-DAS

[20] The Canadian Middle Atmosphere Model (CMAM) is an upward extension of the Canadian Centre for Climate Modeling and Analysis (CCCma) third-generation atmospheric general circulation model (AGCM3). The middle atmosphere component includes comprehensive interactive treatments of stratospheric chemistry, radiative processes and wave-driven dynamics. Detailed descriptions are given by *de Grandpré et al.* [2000] and *Scinocca et al.* [2008]. The chemical module includes all the relevant catalytic ozone loss cycles and heterogeneous reactions on sulphate aerosols and PSCs. It includes parameterizations for Type 1b PSCs (super-cooled ternary solutions, STS) and Type 2 PSCs (water ice), while there is no treatment for Type 1a PSCs (nitric acid trihydrate, NAT particles). Sedimentation of particles is not implemented and thus the model does not simulate denitrification, i.e., the permanent removal of NO_y through the sedimentation of PSC particles in the stratospheric winter polar vortices.

[21] In this work, data are taken from the data assimilation version of the model, CMAM-DAS, and in particular from its recent International Polar Year (IPY) simulation, covering the period February 2007 to August 2009. As opposed to the climate version of the model, CMAM-DAS assimilates the observed day-to-day variations in meteorology, enabling direct comparisons of the simulated chemical species distribution with observations for specific years. CMAM-DAS runs at T47 spectral horizontal resolution (corresponding to roughly 3.75° × 3.75° grid spacing) and employs 71 levels in the vertical, with a resolution that varies from several hundred meters in the lower troposphere to ~1.5 km near 20 km, and ~2.5 km from 60 km to the model lid near 100 km. It uses a 3-D variational assimilation scheme to assimilate observations from surface stations, radiosondes, aircrafts, cloud drift winds and AMSU-A brightness temperatures from the NOAA-15 and NOAA-16 satellites [*Polavarapu et al.*, 2005; *Ren et al.*, 2011].

3.2. GEM-BACH

[22] The GEM-BACH model consists of the Canadian Global Environmental Multiscale (GEM) model in combination with the Belgium Atmospheric CHemistry module (BACH). A detailed description of the model is given by *de Grandpré et al.* [2009]. The model is based on the stratospheric version (GEM-Strato) of the Canadian GEM model [*Côté et al.*, 1998] which has been coupled online with a comprehensive module of stratospheric chemistry developed at BIRA-IASB. The model has 80 levels, including 27 in the stratosphere, and runs at a horizontal resolution of 1.5° with a lid at 0.1 hPa. It uses semi-implicit and semi-Lagrangian numerical techniques optimized to handle a large number of advection equations for the transport of species. Radiative processes are computed according to the correlated-k distribution approach [*Li and Barker*, 2005], which has the accuracy of a line-by-line code.

[23] The Belgium Atmospheric Chemistry module is the foundation of the Belgian Assimilation System of Chemical Observations from the Environmental Satellite (Envisat) chemical transport model (BASCOE CTM) [*Daerden et al.*, 2007] and assimilation system [*Errera et al.*, 2008; *Viscardy et al.*, 2010]. It includes 57 species that interact through 143 gas-phase, 48 photolysis, and 9 heterogeneous reactions. We use here a long run of GEM-BACH realized specifically for the International Polar Year (IPY run) and covering the period from March 2007 to February 2009. In this version, the chemical and photodissociation rates follow the Jet Propulsion Laboratory compilation by *Sander et al.* [2003]. While heterogeneous reactions on the surface of PSCs particles are explicitly taken into account, the surface area available for these reactions is parameterized in a crude manner. Type 2 PSCs (water ice) are set to appear at temperatures below 186 K with a surface area density of 5×10^{-9} cm^2/cm^3. Between 186 K and 194 K, they are replaced by Type Ia (NAT) PSCs with the same surface area density. In this temperature range, the sedimentation of NAT PSCs is represented by an exponential loss of HNO_3 with a characteristic time of 100 days.

3.3. SLIMCAT

[24] The updated Single-Layer Isentropic Model of Chemistry and Transport (SLIMCAT) is a 3-D off-line chemical transport model (CTM) [*Chipperfield*, 2006]. It differs from a general circulation model in that the chemistry component is not integrated into the dynamical model, but is off-line and performed separately for each dynamical time step. This model has been used for many studies of ozone and ozone related gases in the polar regions [e.g., *Chipperfield and Jones*, 1999; *Solomon et al.*, 2002; *Manney et al.*, 2009]. The model uses winds and temperatures from meteorological analyses of the European Centre for Medium-Range Weather Forecasts (ECMWF) to specify the atmospheric transport and temperatures, and calculates the abundances of chemical species in the troposphere and stratosphere. With hybrid σ-θ vertical coordinate levels (terrain-following sigma coordinates combined with isentropic levels in the stratosphere) and a sophisticated radiation scheme (a Delta-Eddington approximation-based radiation scheme [*Joseph et al.*, 1976; *Briegleb*, 1992]), it produces realistic representations of tracer transport.

[25] The simulation analyzed here has 2.8° × 2.8° horizontal resolution, with 50 levels from the surface to 3000 K (~60 km), using purely isentropic surfaces above 350 K. The model uses a limited number of chemical families containing species which are in rapid photochemical equilibrium, in order to reduce the number of gases that must be advected. Reactions are generally computed using the photochemical data of *Sander et al.* [2003], with photolysis rates calculated using a scheme based on work by *Lary and Pyle*

Table 2. Box Model Errors From Scaling to Local Noon, Estimated as Described in the Text

Day	NO	NO_2	HNO_3	N_2O_5	$ClONO_2$	5-NO_y	4-NO_y	NO_x
60	0.031	0.077	0.000	0.041	0.012	0.002	0.002	0.050
90	0.051	0.164	0.001	0.228	0.034	0.020	0.019	0.109
120	0.066	0.096	0.001	0.077	0.024	0.022	0.021	0.082
150	0.065	0.086	0.001	0.097	0.026	0.025	0.025	0.076
180	0.063	0.088	0.001	0.112	0.030	0.027	0.027	0.076
210	0.063	0.099	0.001	0.111	0.034	0.029	0.029	0.080
240	0.054	0.166	0.001	0.126	0.043	0.033	0.033	0.103

[1991]. Reactions occurring on the surface of NAT, liquid STS, and ice PSC particles are included in the SLIMCAT model. Denitrification and dehydration are treated using a simple sedimentation scheme.

4. Model Comparisons

4.1. Methodology

[26] In order to facilitate a consistent comparison between the FTIR and the models, FTIR VMR profiles of NO, NO_2, and $ClONO_2$, which exhibit strong diurnal variations, were scaled to a corresponding noon profile using a photochemical box model [*McLinden et al.*, 2000]. The box model was initialized with monthly mean climatologies of temperature, ozone, NO_y and other long-lived species. A default albedo of 0.7 was assumed. When these assumed values do not correspond to the actual atmospheric values, there will be an error in the scaling. Furthermore, there is a degree of uncertainty associated with all input photochemical rate constants and absorption coefficients.

[27] In order to estimate the error from the scaling to local noon, we considered the worst case—scaling from a SZA of 90° to local noon—since this (generally) represents the largest scaling. This was done for several days throughout the year (days 60–240 in 30 day increments). For polar day, the maximum SZA was used instead of 90°. Each model parameter was varied by a measure of its uncertainty, and the scaling factors were recalculated and compared with the standard values used in the analysis. A list of these parameters and the amount by which they were varied are as follows: temperature: 10 K, ozone: 10%, NO_y: 20%, albedo: 0.5, rate constant $NO+O_3$: 40%, rate constant NO_2+O: 14%, rate constant HNO_3+OH: 20%, $jHNO_3$: 10%, jNO_2: 10%, and jN_2O_5: 10%.

[28] The resultant error for each of these terms was added in quadrature for each NO_y species measured by the FTIR. The total relative error in NO_x or NO_y was then constructed by weighting the total uncertainty for each species by its total column (as simulated in the box model). As both morning and afternoon observations were used, and their scaling factors and uncertainties are not the same, the larger of the two was taken to represent the uncertainty for the day in question. The results are shown in Table 2.

[29] The largest errors occur in NO_2, and to a lesser extent NO and N_2O_5, with the largest contributions from the uncertainty in surface albedo and the photochemical reactions $NO+O_3$ and NO_2+O. The large uncertainty assigned to albedo stems from the variability in snow and/or cloud cover. The behavior of the overall error in NO_y is a result of two main factors: (1) the fraction of the total NO_y column present as HNO_3, which is least sensitive to errors in the input parameters, and which varies with time of year; and (2) the amount by which the scaling factor departs from unity—an indicator of the difference in SZA between 90° and local noon. That is, when local noon occurs at larger SZAs, the scaling is closer to unity and thus not as sensitive to uncertainties in the input parameters. Likewise, when the maximum SZA is smaller than 90°, the required scaling is also closer to unity. The error in NO_x is an overestimate as the error sources that affect the partitioning between NO and NO_2 will largely cancel in their sum. No scaling to noon was performed for HNO_3, whose diurnal variation is negligible compared to the other species. Partial columns were then calculated for each gas, followed by a "daily mean" partial column calculation.

[30] For each model, the VMR profiles were chosen for the model grid point closest to Eureka. The noon model VMR profiles were interpolated on to the FTIR retrieval grid and smoothed by the FTIR averaging kernels and a priori VMR profiles according to the method of *Rodgers and Connor* [2003]:

$$\mathbf{x}_s = \mathbf{x}_a + \mathbf{A}(\mathbf{x}_m - \mathbf{x}_a) \tag{3}$$

where $\mathbf{x}_s$ is the smoothed profile, $\mathbf{x}_a$ is the FTIR a priori profile, $\mathbf{A}$ is the FTIR averaging kernel matrix, and $\mathbf{x}_m$ is the model's VMR profile. The smoothing accounts for the lower vertical resolution and a priori profile of the FTIR measurements when comparing to other measurements or model calculations having higher vertical resolution. Partial columns were then calculated from each smoothed profile, using atmospheric densities provided with each model. For the stratospheric species considered in this study, smoothing typically increases the partial columns, since the averaging kernels are weighted to the stratosphere.

4.2. Results and Discussion

[31] The resulting time series for the smoothed partial columns from the three models were compared with the FTIR measurements. Figure 4 shows the comparisons with CMAM-DAS for NO, NO_2, HNO_3, and $ClONO_2$. The CMAM-DAS NO partial columns match the FTIR columns in early spring but become larger, on average by 16%, during late spring and summer. The CMAM-DAS NO_2 partial columns are consistently larger on average by 8% throughout each year, the difference being most pronounced in the spring of 2007. The CMAM-DAS HNO_3 and $ClONO_2$ partial columns are smaller than the FTIR columns, with the largest differences occurring during summer for HNO_3 and during the spring for $ClONO_2$. The $ClONO_2$ bias is due to a known issue in CMAM-DAS with the partitioning of chlorine reservoir species in the polar vortex, resulting in overestimated HCl mixing ratios and underestimated $ClONO_2$ mixing ratios. The HNO_3 bias is currently not well understood. In a recent comparison of NO_y-N_2O correlations between a variety of coupled chemistry-climate models and data from MIPAS and the NASA ER-2 aircraft [cf. *Eyring et al.*, 2010, Figure 6.14] CMAM showed excellent agreement with the observation. (Note that HNO_3 constitutes the largest fraction of NO_y.) This inconsistency between the

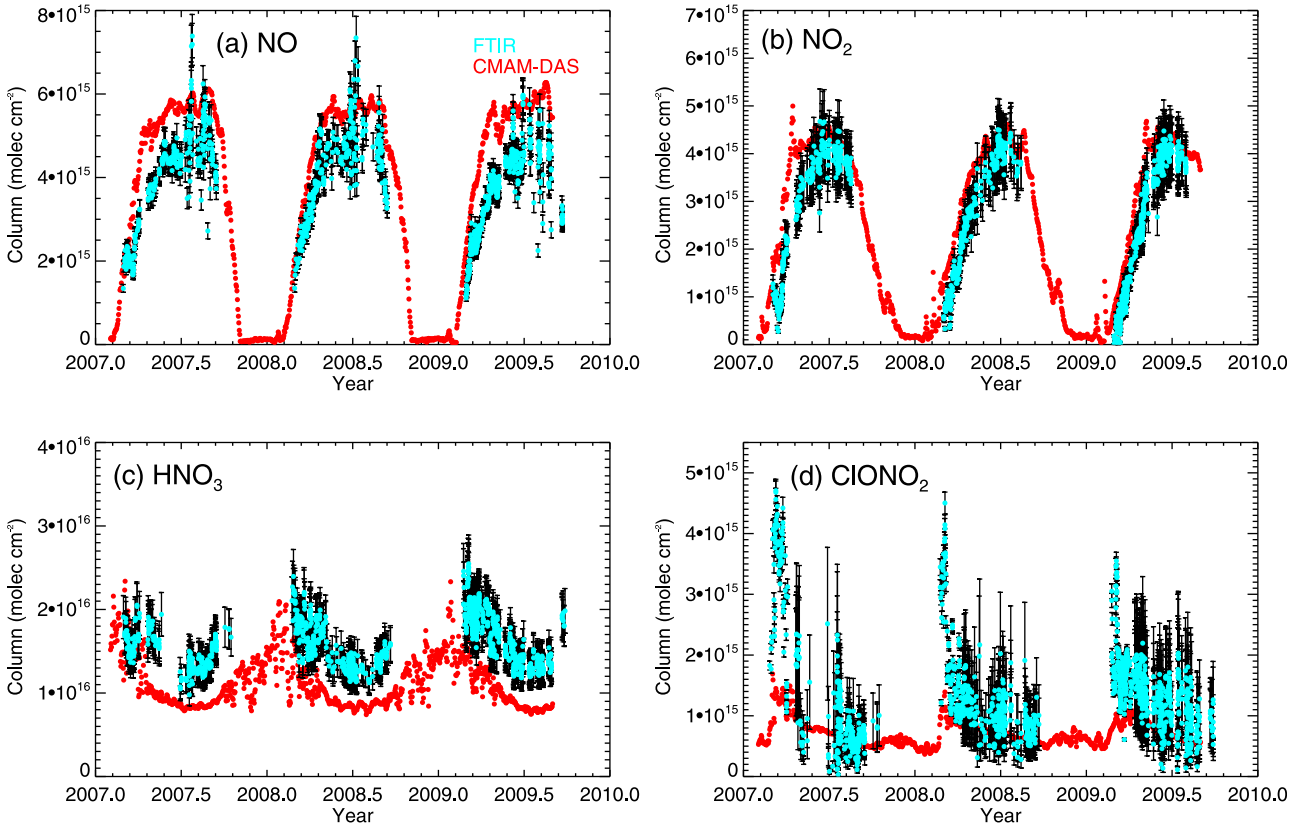

Figure 4. FTIR (cyan) and smoothed CMAM-DAS (red) 15–40 km partial columns for (a) NO, (b) NO_2, (c) HNO_3, and (d) $ClONO_2$. The black vertical bars represent the error for each gas, as shown in Table 1.

Eyring et al. [2010] study and the results presented here needs further analysis.

[32] Similar plots are shown in Figure 5 for GEM-BACH. For NO and NO_2, GEM-BACH has consistently larger partial columns (on average by 18 and 20%, respectively), especially during the summer. The GEM-BACH HNO_3 partial columns match the FTIR well during the spring of 2007, but are slightly smaller than the FTIR for the rest of the comparison period (by approximately 10%). This shows the shortcoming of the GEM-BACH parameterization of denitrification, i.e., irreversible loss of HNO_3 as soon as NAT PSCs appear. For $ClONO_2$, GEM-BACH consistently delivers significantly larger partial columns than observed by the FTIR. This is most probably due to the model neglecting Type Ib PSCs (supercooled ternary solutions), while they play an important role in the wintertime heterogeneous loss of $ClONO_2$ in the Arctic [e.g., *Hanisco et al.*, 2002]. It should be noted that the PSC parameterization in GEM-BACH (see section 3.2) was adjusted for ozone depletion processes above the Antarctic and was not checked previously against Arctic observations.

[33] SLIMCAT partial columns show the best agreement with the FTIR data, as seen in Figure 6. For NO, SLIMCAT matches the measured partial columns very closely, with the exception of some enhanced columns measured in summer. The SLIMCAT NO_2 partial columns are larger than the measurements, by approximately 5% for the entire comparison interval. For HNO_3, the SLIMCAT partial columns agree within approximately 2% with the measured partial columns except during the early springs, when they peak earlier than the FTIR. $ClONO_2$ partial columns agree within approximately 2% during all four spring seasons, but during the summer–fall periods, SLIMCAT partial columns are larger than the measurements. Model comparisons are extremely difficult around the polar vortex edge due to the resolution of the models, and this may be contributing to the difficulty all the models have in capturing the observations at this time of year.

[34] To obtain an estimate of the NO_y partial columns, the partial columns for NO, NO_2, HNO_3, and $ClONO_2$ were added for the FTIR and the three models. This product is henceforth called 4-NO_y. The results are shown in Figure 7. The mean percentage difference between each model and the FTIR measurements was calculated as:

$$\Delta\% = \frac{100}{N}\sum_{i=1}^{N}\left[\left(MODEL_{PC}^{(i)} - FTIR_{PC}^{(i)}\right)/FTIR_{PC}^{(i)}\right] \quad (4)$$

where $FTIR_{PC}^{(i)}$ is the partial column measured by the FTIR and $MODEL_{PC}^{(i)}$ is the partial column simulated by the model, for day i.

[35] Figure 7a compares CMAM-DAS 4-NO_y with the FTIR and shows that the model partial columns generally are smaller than those measured by the FTIR. During the 2007 spring, the partial columns match well, but throughout rest of the period, the model partial columns are consistently smaller than the FTIR columns. Figure 7b shows the mean

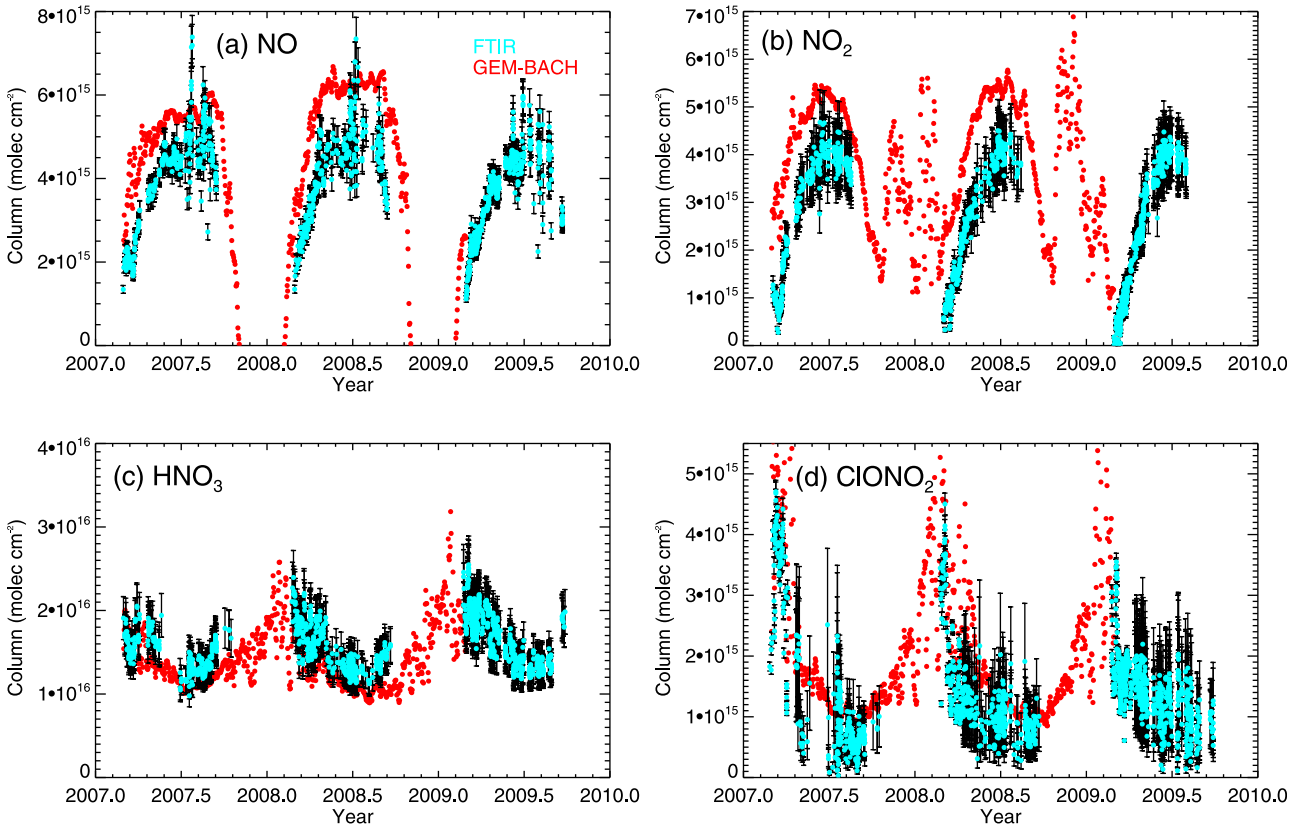

Figure 5. Same as Figure 4 but for the FTIR and smoothed GEM-BACH.

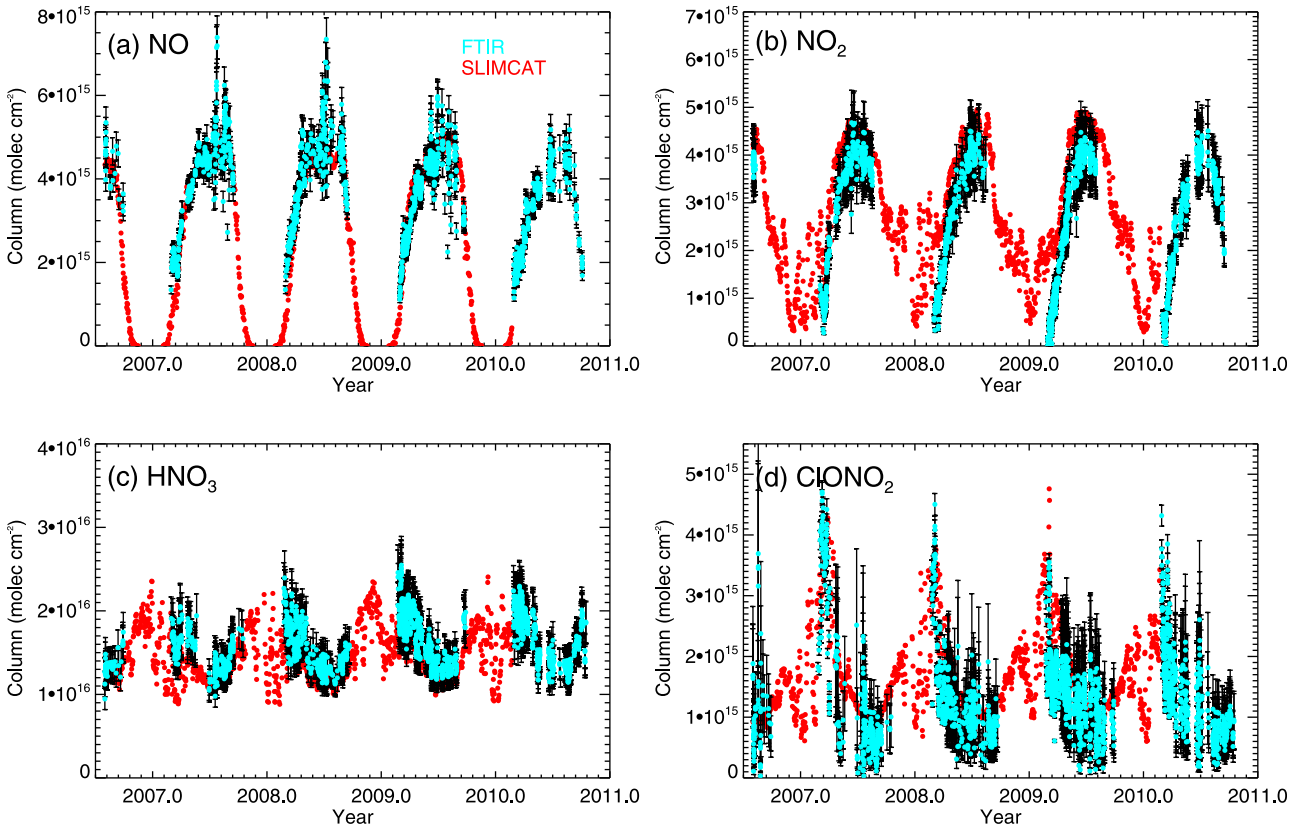

Figure 6. Same as Figure 4 but for the FTIR and smoothed SLIMCAT.

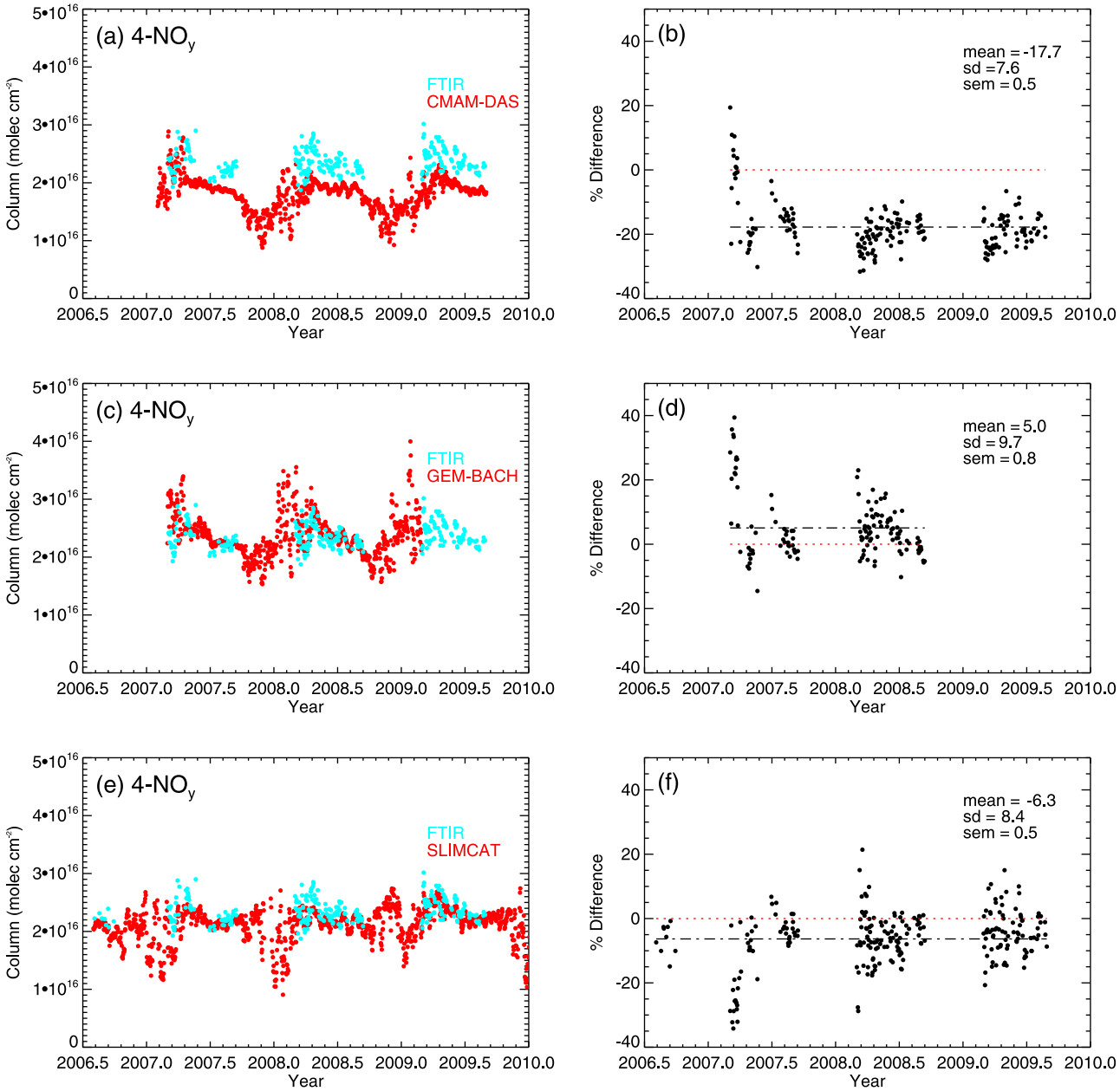

Figure 7. The 4-NO_y ($NO + NO_2 + HNO_3 + ClONO_2$) 15–40 km partial column for the FTIR (cyan) and smoothed model (red): (a) CMAM-DAS, (c) GEM-BACH, and (e) SLIMCAT. The differences for each coincidence: (b) for CMAM-DAS, (d) for GEM-BACH, and (f) for SLIMCAT, along with the mean percentage difference (black dash-dotted line), the standard deviation, and the standard error of the mean relative difference. The red dotted line indicates the zero line.

percentage difference for the compared pairs, $(-17.7 \pm 0.5)\%$, where the given error, here and henceforth throughout the paper, is the standard error of the mean. The standard error of the mean relative difference between the model and FTIR partial column (*sem*, in percent) has been evaluated as $sd/\sqrt{N}$, in which *sd* is the statistical 1-sigma (1σ) standard deviation of the observed differences, and N is the number of coincidences. The *sem* provides a measure of the significance of an observed bias [*De Mazière et al.*, 2008]. The standard deviation about the mean, 7.6%, is also shown. For this comparison, the negative bias is a consequence of the low bias in the CMAM-DAS HNO_3 partial columns (Figure 4), as HNO_3 dominates the NO_y budget.

[36] For the GEM-BACH comparison seen in Figure 7c, the agreement with the FTIR is good. There is a slight positive bias of $(5.0 \pm 0.8)\%$ (Figure 7d), indicating that the model partial columns are slightly larger. The standard deviation in this case is 9.7%. For the SLIMCAT comparison (Figure 7e) the model partial columns are smaller than those measured by the FTIR during the spring of each year, and better match the measurements during the summer. The mean bias in this case is negative, $(-6.3 \pm 0.5)\%$, as shown in Figure 7f, with a standard deviation of 8.4%. For the

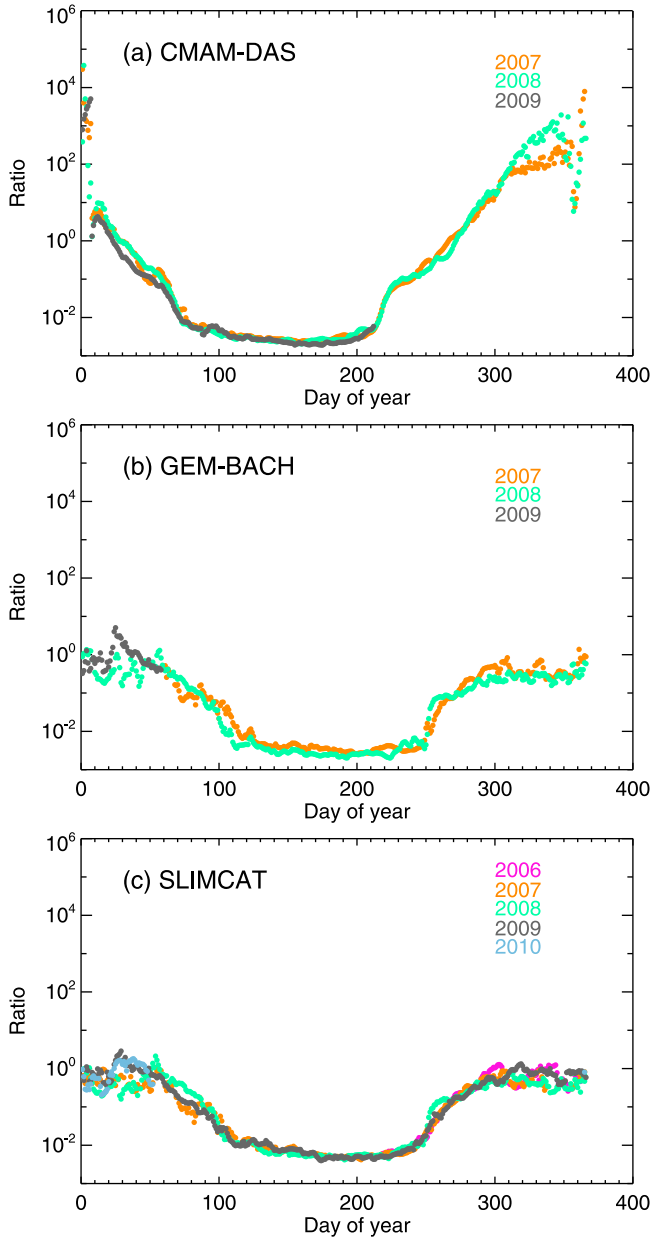

Figure 8. N_2O_5/NO_x ratios for (a) CMAM-DAS, (b) GEM-BACH, and (c) SLIMCAT. The colors correspond to different years as indicated in the legend.

4-NO_y data product, the mean percentage differences relative to the measurements for SLIMCAT and GEM-BACH are similar, being within the mean total (measurement + scaling) error of 9.5%. For CMAM-DAS, the mean difference is larger than the mean total error.

[37] We note large differences among the models during the first two months of 2008 and 2009. During these wintertime periods, GEM-BACH delivers notably higher values than the two other models. This is due to the simplistic PSC parameterization in GEM-BACH, which does not allow any segregation between gas-phase and condensed HNO_3. Hence the HNO_3 abundances used for this model are total abundances, including both the gaseous and condensed phase, while for the other two models gas-phase HNO_3 are used.

[38] The FTIR measures four of the five NO_y primary species: NO, NO_2, HNO_3, and $ClONO_2$. Since N_2O_5 also contributes significantly to the Arctic NO_y budget, as shown in Figure 1, we used the simulated N_2O_5/NO_x partial column ratios from the models discussed above to calculate N_2O_5. The resulting NO_y product, including all five primary NO_y species (henceforth called 5-NO_y), was derived as follows:

$$5\text{-}NO_y^{FTIR} = NO^{FTIR} + NO_2^{FTIR} + HNO_3^{FTIR} + ClONO_2^{FTIR} + 2 \times (N_2O_5^{model}/NO_x^{model}) \times NO_x^{FTIR} \quad (5)$$

where $N_2O_5^{model}/NO_x^{model}$ is the model ratio, and NO_x^{FTIR} is the measured NO_x partial column. Figure 8 shows these ratios calculated for each model. For all three models, the summer ratios are near zero due to 24 h daylight and hence very similar, however differences are seen for early spring and fall–winter, with CMAM-DAS ratios significantly higher than those from GEM-BACH and SLIMCAT. This discrepancy is most likely due to the less detailed transport scheme in CMAM-DAS as compared to the other models. While GEM-BACH transports every species separately and SLIMCAT transports all nitrogen species separately except NO_x (NO + NO_2), in CMAM-DAS four of the shorter-lived nitrogen species (NO + NO_2 + NO_3 + 2 × N_2O_5) are transported together. Bulk-transport by chemical family is done generally to minimize the computational cost of a transport scheme and to avoid strong gradients in advected fields. This means that after each transport step in the model, the advected family is split apart into its individual family members using the partitioning ratios saved on the grid during the previous time step. The partitioning between NO and NO_2 is very fast and completely dependent on sunlight, so the NO concentration goes to zero in the night in all three models. But the partitioning between NO_x and the longer-lived species; e.g., N_2O_5 and HNO_3, is slower. Both GEM-BACH and SLIMCAT see substantial values of NO_2 in the polar night, which is evidence of air masses that have recently been exposed to sunlight. Since in CMAM-DAS the partitioning is locked down on to the model grid, nitrogen oxides from lower latitudes can be advected into the polar night but when the advected quantity is split apart into the separate species, the partitioning will be that of an air mass that has been in the dark for a long time, which explains why CMAM-DAS displays near-zero NO_2 (Figure 4) and an anomalous N_2O_5/NO_x ratio throughout the winter (Figure 8).

[39] The CMAM-DAS, GEM-BACH, and SLIMCAT results for 5-NO_y are similar to those for 4-NO_y, with mean differences of (−16.0 ± 0.6)%, (5.5 ± 1.0)%, and (−5.8 ± 0.4)%, and standard deviations of 9.4, 12.0, and 7.6% respectively. Again, the mean percentage differences relative to the measurements for GEM-BACH and SLIMCAT are within the mean total error (measurement + scaling) of 9.6%, while those for CMAM-DAS are larger.

5. ACE-FTS Comparisons

5.1. Methodology

[40] The methodology for comparing ACE-FTS data with the FTIR was described by *Batchelor et al.* [2010]. In brief, the following filtering criteria were applied to the VMR profiles: a time difference of less than ±12 h, a spatial

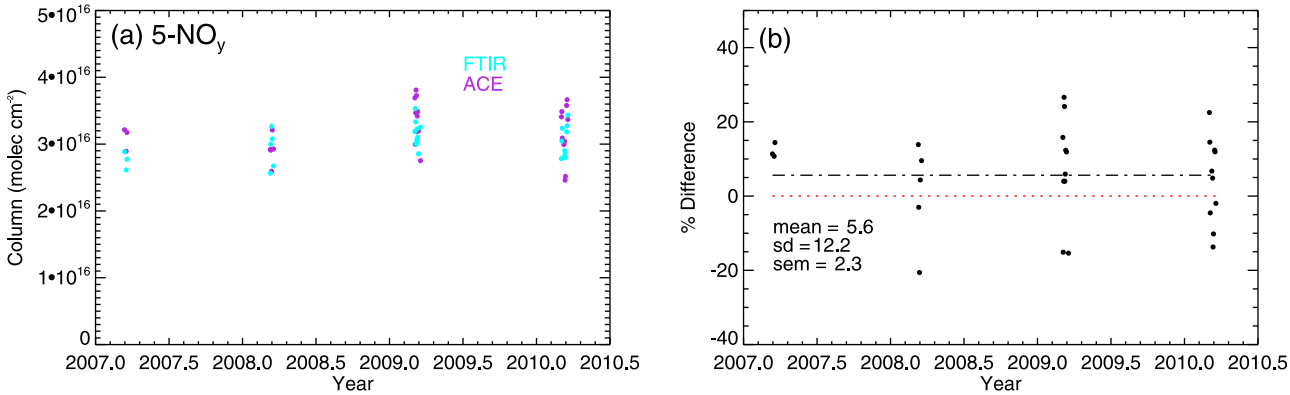

Figure 9. (a) 5-NO_y 15–40 km partial columns for the FTIR (cyan) and smoothed ACE-FTS (purple); (b) differences calculated for each coincidence. The mean percentage difference (black dash-dotted line), the standard deviation, and the standard error of the mean are also shown. The red dotted line indicates the zero line.

difference of ≤1000 km, and a maximum temperature difference of <10 K between the sampled air masses at each altitude between 15 and 40 km. In addition, the scaled potential vorticity (sPV) differences between the FTIR and ACE-FTS at each altitude along the line-of-sight were restricted to less than 0.3×10^{-4} s^{-1}, ensuring that the sampled air masses were similar for both measurements relative to the polar vortex edge. sPV was derived for both ACE-FTS and FTIR at locations along the line-of-sight using the GEOS Version 5.0.1 (GEOS-5) analyses [*Reinecker et al.*, 2008]. sPV is the PV scaled in vorticity units, providing a field with a similar range of values at altitudes throughout the stratosphere [e.g., *Dunkerton and Delisi*, 1986; *Manney et al.*, 1994; *Manney et al.*, 2007, and references therein]. An sPV value of 1.2×10^{-4} s^{-1} was used as a proxy for the outer edge of the polar vortex and an sPV value of 1.6×10^{-4} s^{-1} was used for the inner edge, as these values are typically in the vortex edge region in the stratosphere [*Manney et al.*, 2008].

[41] For all coincident ACE-FTS NO, NO_2, and $ClONO_2$ profiles, a scaling to noon was also performed to account for the diurnal variation of these species. The ACE-FTS profiles were then interpolated on to the FTIR retrieval grid and smoothed by the FTIR averaging kernels and a priori profiles, using equation (3). Partial columns were calculated for the altitude range 15–40 km to match the FTIR partial columns, and finally, the "daily mean" partial columns were derived for those cases when more than one ACE-FTS measurement was found for a particular day. The 4-NO_y and 5-NO_y were then calculated for both the FTIR and ACE-FTS. To calculate 5-NO_y for the FTIR, the ACE-FTS N_2O_5/NO_x ratios were used, applying equation (5), where the model ratio was replaced by the ACE-FTS ratio.

5.2. Results and Discussion

[42] The quality of the ACE-FTS measurements has been demonstrated by previous studies. *Kerzenmacher et al.* [2008] provide an assessment of ACE-FTS v2.2 NO and NO_2. A companion paper by *Wolff et al.* [2008] provides an assessment of the quality of ACE-FTS v2.2 HNO_3, $ClONO_2$, and the ACE-FTS v2.2 N_2O_5 update. Both studies included comparisons with globally distributed ground-based FTIR spectrometers affiliated with the Network for the Detection of Atmospheric Composition Change (NDACC). For the comparisons of ACE-FTS NO partial columns with six ground-based FTIRs, the mean differences (ACE-FTS − FTIRs) were between −14.5 and −67.5%, becoming more negative from South to North [*Kerzenmacher et al.*, 2008]. Partial column comparisons for NO_2 showed a mean difference of +7.3% between the ACE-FTS instrument and the same six ground-based FTIR spectrometers.

[43] For HNO_3, the comparison with nine ground-based FTIRs showed an agreement within the range −12.6 to +6.0% [*Wolff et al.*, 2008]. For $ClONO_2$, the same study showed an agreement within the range −8.8% to +8.9%. For N_2O_5, there are no comparisons with ground-based FTIRs, but the comparison with MIPAS on ENVISAT using the Institut für Meteorologie und Klimaforschung and Instituto de Astrofísica de Andalucía (IMK-IAA) data processor showed a low bias of the ACE-FTS relative to MIPAS IMK-IAA of −0.25 ppbv at an altitude of 30 km (the altitude of maximum N_2O_5). The mean absolute differences at lower altitudes (16–27 km) were found to be typically −0.05 ppbv for MIPAS nighttime and ±0.02 ppbv for MIPAS daytime measurements [*Wolff et al.*, 2008].

[44] For the 5-NO_y product, approximately two years of overlap between Odin and ACE permitted the comparison of Odin NO_y climatology [*Brohede et al.*, 2008] with an ACE-FTS climatology [*Jones et al.*, 2011]. The comparison was made for pressure surfaces up to 1 hPa and gave absolute differences better than 2 ppbv, equivalent to relative differences less than 20%.

[45] Figure 9a shows the comparison between ACE-FTS and the FTIR 5-NO_y partial columns using all coincidences between 2007 and 2010. Figure 9b shows the percentage differences between the two instruments (ACE-FTS − FTIR)/FTIR. There were fewer coincidences for 2007 and 2008 than for 2009 and 2010. This is a consequence of the number of FTIR spectra acquired during each spring campaign, which is influenced by the local meteorological conditions at Eureka. Table 3 gives the breakdown of the mean percentage differences, the standard deviation, and the standard error on the mean by year. For both 4-NO_y and 5-NO_y, 2007 was a year when the polar vortex was located

Table 3. Summary of the ACE-FTS Versus FTIR Mean Percentage Difference (100 × (ACE-FTS − FTIR)/FTIR), Standard Deviation, Standard Error on the Mean, and Number of Coincidences, N, for the 4-NO_y and 5-NO_y Data Products

	4-NO_y			5-NO_y			
	Mean % Difference	Standard Deviation (%)	Standard Error of Mean (%)	Mean % Difference	Standard Deviation (%)	Standard Error of Mean (%)	N
2007	13.6	2.8	1.6	12.2	2.0	1.1	3
2008	9.1	9.1	4.1	0.8	13.5	6.0	5
2009	6.9	7.1	2.2	7.4	14.2	4.5	10
2010	6.8	3.1	1.0	4.2	11.6	3.7	10
TOTAL	8.0	6.1	1.2	5.6	12.3	2.3	28

above Eureka for more than 10 days. For these coincidences, the ACE-FTS measurements were consistently larger than those of the FTIR, as shown in Figure 9b. During the following years, the instruments sampled most of the time through the vortex edge and the comparisons show both positive and negative differences. Overall, there is a positive mean bias for all years, with ACE-FTS higher than the FTIR. Results for 4-NO_y and 5-NO_y are similar, except for 2008, for which the 5-NO_y difference (0.8%) is much smaller than that for 4-NO_y (9.1%). Over the entire comparison period, the mean percentage difference for 5-NO_y is (5.6 ± 2.3)%, with a standard deviation of 12.2%. This agreement between the ACE-FTS and the FTIR provides confidence in the NO_y product derived from ground-based FTIR measurements at Eureka.

6. Seasonal and Interannual Variability of NO_y

[46] To assess the seasonal and interannual variability of NO_y above Eureka, we used the 5-NO_y calculated using the SLIMCAT N_2O_5/NO_x ratio. The motivation for this choice was that SLIMCAT provided the longest model data set, with a ratio that was consistent with GEM-BACH. Figure 10 shows the FTIR time series of the 5-NO_y partial columns for each year, beginning in August 2006 and ending in October 2010. Variability is greatest during the spring, decreasing in summer and fall. Considering the period up to day 140, we find a mean partial column ($\pm 1\sigma$) of $(2.5 \pm 0.2) \times 10^{16}$ molec cm^{-2}, while for all days after 140, we find a mean partial column of $(2.3 \pm 0.1) \times 10^{16}$ molec cm^{-2}. This shows that the spring mean is higher by approximately 8%, while the spring variability, indicated by the standard deviation, is twice that of the summer and fall. The more scattered partial columns can be explained by more dynamically active meteorological conditions during spring compared to the summer, with the higher partial column values driven by the subsidence of NO_y-rich air from above the partial column range into the column inside the polar vortex.

[47] To investigate the springtime evolution of NO_y, Figure 11 shows the time series for 5-NO_y and its constituent species, along with the sPV for 2007–2010. Figures 11a (top)–11d (top) show the NO_y partial columns together with those of HNO_3, since its contribution is the largest. For all four years, it is evident that the variability of the 5-NO_y partial

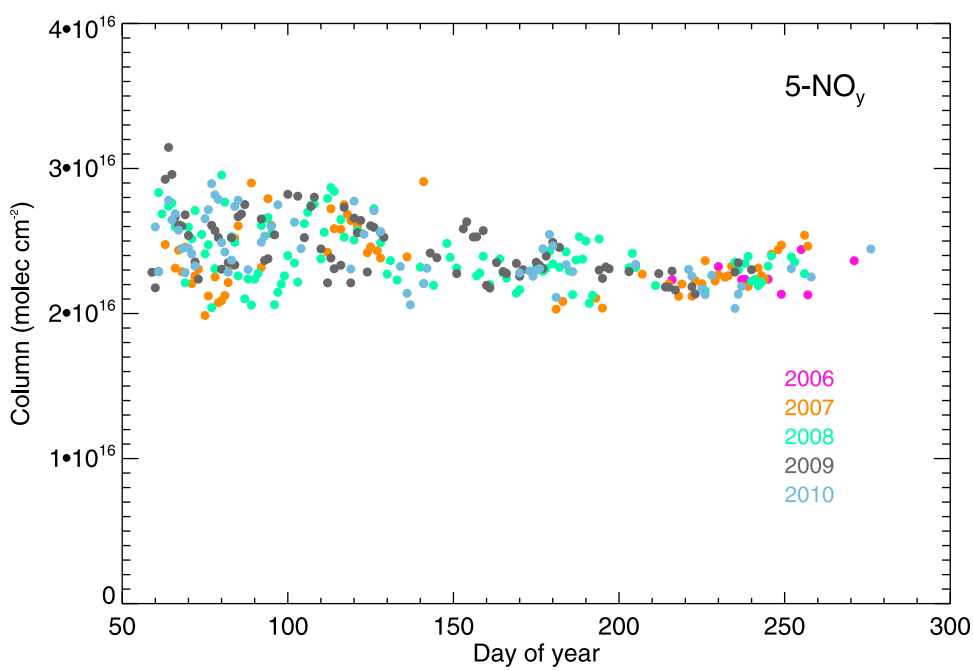

Figure 10. FTIR 15–40 km partial columns of 5-NO_y for the years indicated in the legend.

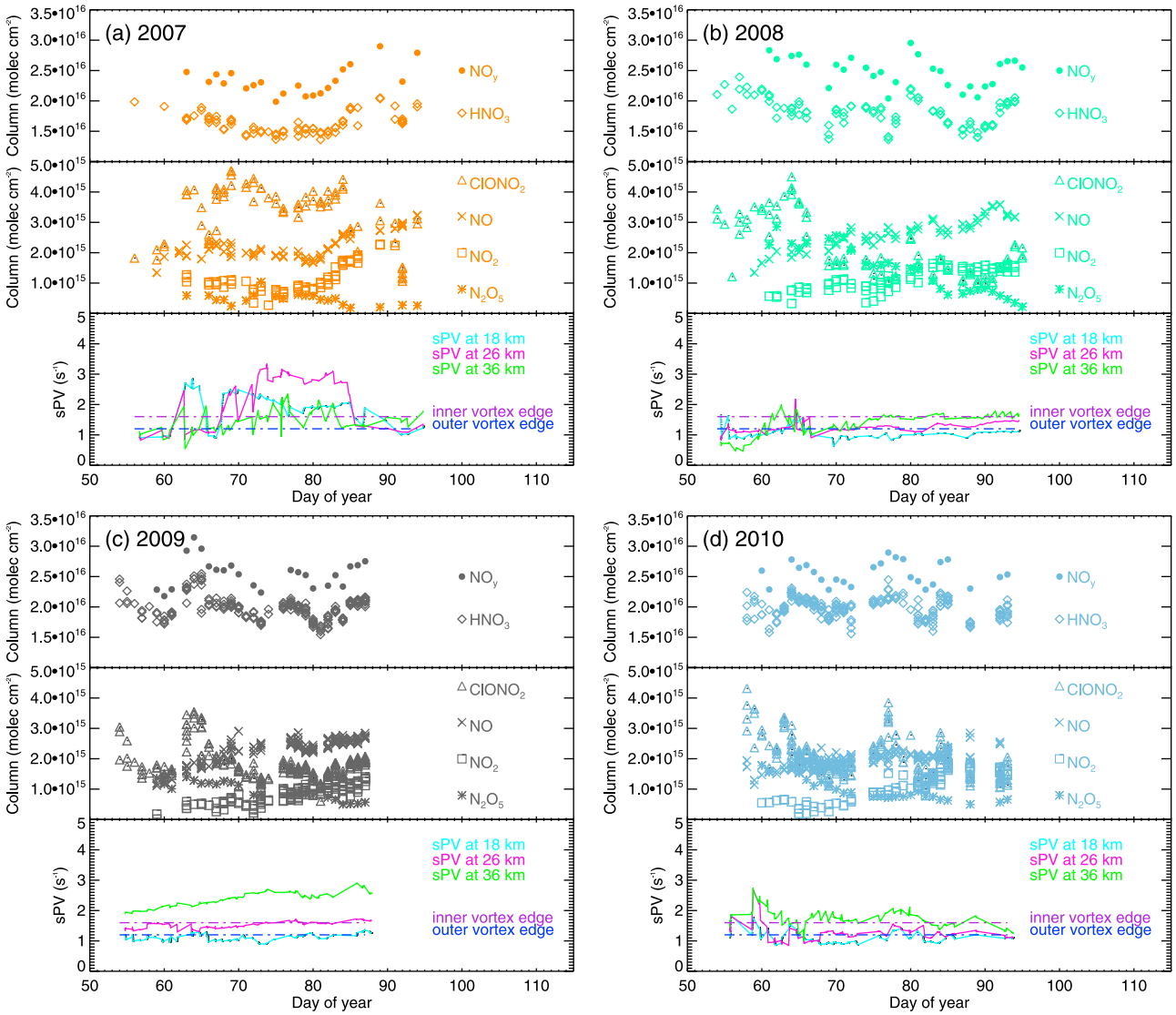

Figure 11. FTIR 15–40 km partial columns of 5-NO_y and constituent species, derived for the spring (a) 2007, (b) 2008, (c) 2009, and (d) 2010. The colors match those in Figure 10. (top) The partial columns of 5-NO_y and HNO_3, and (middle) the partial columns of $ClONO_2$, NO, NO_2, and N_2O_5. (bottom) The evolution of sPV for three altitudes: 18 km (cyan), 26 km (pink), and 36 km (green). The dash-dot lines mark the inner (purple) and outer (blue) vortex edge.

columns is dominated by the variability in the HNO_3 column. Figures 11a (middle)–11d (middle) show the other four NO_y species. In Figures 11a (bottom)–11d (bottom), the evolution of the sPV is given for the 18, 26, and 36 km altitude levels, corresponding to the lower and middle stratosphere. The horizontal distances at 18 and 36 km altitude are less than 1 km at a solar zenith angle of 87°.

[48] The 2006/2007 winter Arctic vortex was particularly strong and cold, resulting in significant destruction of stratospheric ozone [*Rösevall et al.*, 2007; *World Meteorological Organization* (*WMO*), 2011]. After sunrise, occurring on 20 February at Eureka, the FTIR sampled the atmosphere inside the polar vortex for most of the spring, as can be seen from the evolution of sPV. These measurements are consistent with our understanding of the chemical processes that occur in the dynamically isolated air within the vortex, whereby HNO_3-containing PSCs form during cold winters, chlorine is released from its reservoirs (HCl and $ClONO_2$) to participate in springtime ozone destruction, and the resulting springtime repartitioning of chlorine in the Arctic results in enhanced $ClONO_2$ for some time after PSCs have disappeared [*Dufour et al.*, 2006; *WMO*, 2007; *Santee et al.*, 2008]. High $ClONO_2$ columns were measured inside the vortex during 2007 (Figure 11), showing that active chlorine started to return into its reservoirs. This is consistent with the evolution of $ClONO_2$ and HCl measured by *Batchelor et al.* [2010] for this period. Also in the 2007 spring, we see that the HNO_3 partial columns are smaller inside the vortex compared to the vortex edge. Usually, if the vortex is not perturbed by PSC formation, HNO_3 concentrations are large and well correlated with PV [*Santee et al.*, 1999]. In 2007, vortex temperatures (not shown) were favorable for PSC

formation, reaching values below the type II PSC threshold in December and January, and below the type I PSC threshold through 21 March. However, radiosonde measurements above Eureka never fell below 198 K during our measurement campaign. The low HNO_3 values measured at Eureka are thought to be a consequence of HNO_3 being removed from the gas phase in liquid/solid PSC particles elsewhere in the vortex, with this HNO_3-poor air being transported over Eureka. Figure 11a also shows the evolution of NO_x species and N_2O_5. As the days become longer, more NO and NO_2 form from the nighttime reservoir, N_2O_5, through photolysis, implying that the evolution of the N_2O_5 partial columns is opposite to that of NO and NO_2.

[49] During the following years, the instrument sampled mostly through the edge of, or outside, the polar vortex, as seen in the sPV plots in Figure 11 for 2008, 2009, and 2010. The year 2008 was another cold winter, with significant chemical processing [*WMO*, 2011]. The years 2009 and 2010 were both characterized by a strong and prolonged sudden stratospheric warming (SSW) in late January, with no chemical processing and Cl deactivated after early February. The evolution of NO_y shows some temporal variability within each of these years, which is mostly a consequence of dynamics. Some peaks in the $ClONO_2$ partial columns coincide with larger sPV values, corresponding to measurements inside the polar vortex. Some examples are day 64 in 2008, and days 58, 59, and 77 in 2010. During 2009, enhanced partial columns of HNO_3, $ClONO_2$, and N_2O_5 can be seen near day 63, when the sampled layers were on the vortex edge rather than inside the vortex. This is again a consequence of the buildup at the vortex edge, as discussed above. Similar peaks were also seen in the total columns of O_3, HCl, and HF for those days (not shown here). Each year, the photolysis of HNO_3 and N_2O_5 to NO and NO_2 is observed, with low NO and NO_2 in early spring, increasing as the days become longer, as shown above.

7. Conclusions

[50] A four year time series of the total reactive nitrogen (NO_y) stratospheric partial columns (15–40 km) above Eureka, Nunavut, has been obtained using measurements made by a Bruker 125HR FTIR spectrometer. Four components of the NO_y budget were measured (NO, NO_2, HNO_3, $ClONO_2$), while N_2O_5 was derived using model ratios of N_2O_5/NO_x for the closest grid point to Eureka. For the four individual NO_y species, the SLIMCAT model results showed the best agreement with the FTIR measurements. Comparisons of 5-NO_y ($NO + NO_2 + HNO_3 + ClONO_2 + 2 \times N_2O_5$) with three atmospheric models were also made. The comparison showed that the CMAM-DAS 5-NO_y partial columns were smaller than the FTIR partial columns, the mean percentage difference ($100 \times$ (model − FTIR)/FTIR) being (-16.0 ± 0.6)% (where the uncertainty represents the standard error of the mean). GEM-BACH 5-NO_y showed an agreement of (5.5 ± 1.0)%, with the model partial columns being slightly larger than the FTIR columns. For the SLIMCAT chemical transport model, the 5-NO_y partial columns were slightly smaller than the FTIR columns, the mean percentage difference being (-5.8 ± 0.4)%. For GEM-BACH and SLIMCAT, the differences were found to be within the mean total (measurement + scaling) error of 9.6%, while the CMAM-DAS difference was larger than the mean total error estimated for the 5-NO_y.

[51] The FTIR measurements were further compared with ACE-FTS springtime measurements, a period when ACE has overpasses above Eureka. Data from four Canadian Arctic ACE Validation Campaigns at Eureka were compared using strict coincidence criteria to constrain time, distance, temperature, and sPV at altitudes along the lines-of-sight for both instruments for the compared air masses. For 5-NO_y, a mean percentage difference of (5.6 ± 2.3)% was found, indicating that the ACE-FTS partial columns are slightly larger than the FTIR columns. The small difference shows that the two instruments are in good agreement, despite their different viewing geometries and the high variability of the springtime Arctic stratosphere.

[52] The seasonal and interannual variability of 5-NO_y above Eureka was also investigated. The 5-NO_y partial column was approximately constant through the sunlit part of the year, from mid-February to mid-October, with greater variability during the spring. The mean partial column averaged for the spring period (up to day 140) was $(2.5 \pm 0.2) \times 10^{16}$ molec cm^{-2}, while for the period after day 140, it was $(2.3 \pm 0.1) \times 10^{16}$ molec cm^{-2}. The springtime evolution of 5-NO_y and its constituent nitrogen species, along with sPV, was examined for all four years. The variability of the 5-NO_y partial column was seen to be dominated by that of HNO_3. The evolution of the individual nitrogen species was found to be consistent with the current understanding of the chemical and dynamical processes that occur in the polar stratosphere. The NO_y data product derived in this study can be further used to validate the ACE-FTS v.3 NO_y. In the longer term, this data product can be also used for trend studies, contributing to a better understanding of the future evolution of NO_y.

[53] **Acknowledgments.** The authors wish to thank the staff at the Eureka weather station and CANDAC for the logistical and on-site support provided at Eureka. They also thank CANDAC/PEARL Operations Manager Pierre Fogal, and Ashley Harrett, Alexei Khmel, Paul Loewen, Keith MacQuarrie, Oleg Mikhailov, and Matt Okraszewski, the CANDAC operators, for their invaluable assistance in maintaining the instrument and taking measurements. CANDAC and PEARL are funded by the Atlantic Innovation Fund/Nova Scotia Research Innovation Trust, the Canadian Foundation for Climate and Atmospheric Sciences, the Canadian Foundation for Innovation, the Canadian Space Agency (CSA), Environment Canada (EC), Government of Canada International Polar Year funding, the Natural Sciences and Engineering Research Council (NSERC), the Ontario Innovation Trust, the Polar Continental Shelf Program, and the Ontario Research Fund. The authors wish to thank the CMAM-DAS group members Stephen Beagley, Michael Neish, Yulia Nezlin, Saroja Polavarapu, Shuzhan Ren, Yves Rochon, and Theodore Shepherd for their efforts to produce the analysis and for making the results available, and David Plummer at Environment Canada for helping us interpret some of the CMAM biases. We also thank Keeyoon Sung for his work compiling the a priori profiles and covariance matrices used in the FTIR retrievals. The Atmospheric Chemistry Experiment, also known as SCISAT, is a Canadian-led mission mainly supported by the CSA and NSERC. The Canadian Arctic ACE validation campaigns are supported by the CSA, EC, NSERC, and the Northern Scientific Training Program.

References

Batchelor, R. L., K. Strong, R. Lindenmaier, R. Mittermeier, H. Fast, J. R. Drummond, and P. F. Fogal (2009), A new Bruker IFS 125HR FTIR spectrometer for the Polar Environment Atmospheric Research Laboratory at Eureka, Canada: Measurements and comparison with the existing Bomem DA8 spectrometer, *J. Atmos. Oceanic Technol.*, *26*(7), 1328–1340, doi:10.1175/2009JTECHA12151.

Batchelor, R. L., F. Kolonjari, R. Lindenmaier, R. L. Mittermeier, W. Daffer, H. Fast, G. Manney, K. Strong, and K. A. Walker (2010), Four Fourier Transform Spectrometers and the Arctic Polar Vortex: Instrument intercomparison and ACE-FTS validation at Eureka during the IPY springs of 2007 and 2008, *Atmos. Meas. Tech.*, *3*, 51–66.

Bernath, P. F., et al. (2005), Atmospheric Chemistry Experiment (ACE): Mission overview, *Geophys. Res. Lett.*, *32*, L15S01, doi:10.1029/2005GL022386.

Boone, C. D., R. Nassar, K. A. Walker, Y. Rochon, S. D. McLeod, C. P. Rinsland, and P. F. Bernath (2005), Retrievals for the Atmospheric Chemistry Experiment Fourier Transform Spectrometer, *Appl. Opt.*, *44*, 7218–7231.

Briegleb, B. P. (1992), Delta-Eddington approximation for solar radiation in the NCAR Community Climate Model, *J. Geophys. Res.*, *97*(D7), 7603–7612.

Brohede, S., C. A. McLinden, G. Berthet, C. S. Haley, D. Murtagh, and C. Sioris (2007), A stratospheric NO_2 climatology from Odin/OSIRIS limb-scatter measurements, *Can. J. Phys.*, 1253–1274, doi:10.1139/P07–141.

Brohede, S., C. A. McLinden, J. Urban, C. S. Haley, A. I. Jonsson, and D. Murtagh (2008), Odin stratospheric proxy NO_y measurements and climatology, *Atmos. Chem. Phys.*, *8*, 5731–5754.

Chipperfield, M. P. (2006), New version of the TOMCAT/SLIMCAT off-line chemical transport model: Intercomparison of stratospheric traces experiments, *Q. J. R. Meteorol. Soc.*, *132*, 1179–1203, doi:10.1256/qj.05.51.

Chipperfield, M. P., and R. L. Jones (1999), Relative influences of atmospheric chemistry and transport on Arctic ozone trends, *Nature*, *400*, 551–554.

Côté, J., S. Gravel, A. Méthot, A. Patoine, M. Roch, and A. Staniforth (1998), The operational CMC–MRB Global Environmental Multiscale (GEM) model. Part I: Design considerations and formulation, *Mon. Weather Rev.*, *126*, 1373–1395.

Daerden, F., N. Larsen, S. Chabrillat, Q. Errera, S. Bonjean, D. Fonteyn, K. Hoppel, and M. Fromm (2007), A 3D CTM with detailed online PSC microphysics: Analysis of the Antarctic winter 2003 by comparison with satellite observations, *Atmos. Chem. Phys.*, *7*, 1755–1772.

Danilin, M. Y. I., M. Koike, G. K. Yue, N. B. Jones, and P. V. Johnston (1999), Nitrogen species in the post-Pinatubo stratosphere: Model analysis utilizing UARS measurements, *J. Geophys. Res.*, *104*(D7), 8247–8262, doi:10.1029/1999JD900024.

de Grandpré, J., S. R. Beagley, V. I. Fomichev, E. Griffioen, J. C. McConnell, A. S. Medvedev, and T. G. Shepherd (2000), Ozone climatology using interactive chemistry: Results from the Canadian middle atmosphere model, *J. Geophys. Res.*, *105*(D21), 26,475–26,491.

de Grandpré, J., R. Ménard, Y. J. Rochon, C. Charette, S. Chabrillat, and A. Robichaud (2009), Radiative impact of ozone on temperature predictability in a coupled chemistry-dynamics data assimilation system, *Mon. Weather Rev.*, *137*, 679–692, doi:10.1175/2008MWR2572.1.

De Mazière, M., et al. (2008), Validation of ACE-FTS v2.2 methane profiles from the upper troposphere to the lower mesosphere, *Atmos. Chem. Phys.*, *9*, 2421–2435.

Dibb, J. E., E. Scheuer, M. Avery, J. Plant, and G. Sachse (2006), In situ evidence for renitrification in the Arctic lower stratosphere during the polar aure validation experiment (PAVE), *Geophys. Res. Lett.*, *33*, L12815, doi:10.1029/2006GL026243.

Dufour, G., et al. (2006), Partitioning between the inorganic chlorine reservoirs HCl and ClONO2 during the Arctic winter 2005 from the ACE-FTS, *Atmos. Chem. Phys.*, *6*, 2355–2366, doi:10.5194/acp-6-2355-2006.

Dunkerton, T. J., and D. P. Delisi (1986), Evolution of potential vorticity in the winter stratosphere of January–February 1979, *J. Geophys. Res.*, *91*, 1199–1208.

Errera, Q., F. Daerden, S. Chabrillat, J. C. Lambert, W. A. Lahoz, S. Viscardy, S. Bonjean, and D. Fonteyn (2008), 4D-Var assimilation of MIPAS chemical observations: Ozone and nitrogen dioxide analyses, *Atmos. Chem. Phys.*, *8*, 6169–6187.

Eyring, V., T. G. Shepherd, and D. W. Waugh (2010) SPARC report on the evaluation of chemistry-climate models, *WMO/TD 1526*, World Meteorol. Org., Geneva, Switzerland.

Fahey, D. W., D. M. Murphy, K. K. Kelly, M. K. W. Ko, M. H. Proffitt, C. S. Eubank, G. V. Ferry, M. Lowenstein, and K. R. Chan (1989), Measurements of nitric oxide and total reactive nitrogen in the Antarctic stratosphere: Observations and chemical implications, *J. Geophys. Res.*, *94*(D14), 16,665–16,681.

Farahani, E. E., et al. (2007), Nitric acid measurements at Eureka obtained in winter 2001–2002 using solar and lunar Fourier transform absorption spectroscopy: Comparisons with observations at Thule and Kiruna and with results from three-dimensional models, *J. Geophys. Res.*, *112*, D01305, doi:10.1029/2006JD007096.

Forster, P., et al. (2007), Changes in atmospheric constituents and in radiative forcing, in *Climate Change 2007: The Physical Scientific Basis, Contribution of Working Group I to the Fourth Assessment Report of the Intergovernmental Panel on Climate Change*, edited by S. Solomon et al., pp. 129–234, Cambridge Univ. Press, Cambridge, U. K.

Gille, J. C., and J. M. I. Russell (1984), The Limb Infrared Monitor of the Stratosphere: Experiment description, performance, and results, *J. Geophys. Res.*, *89*(D4), 5125–5140, doi:10.1029/JD089iD04p05161.

Gordley, L. L., et al. (1996), Validation of nitric oxide and nitrogen dioxide measurements made by the Halogen Occultation Experiment for UARS platform, *J. Geophys. Res.*, *101*(D6), 10,241–10,266, doi:10.1029/95JD02143.

Griesfeller, A., J. Griesfeller, F. Hase, I. Kramer, P. Loës, S. Mikuteit, U. Raffalski, T. Blumenstock, and H. Nakajima (2006), Comparison of ILAS-II and ground-based FTIR measurements of O_3, HNO_3, N_2O, and CH_4 over Kiruna, Sweden, *J. Geophys. Res.*, *111*, D11S07, doi:10.1029/2005JD006451.

Grossel, A., N. Huret, V. Catoire, G. Berthet, J.-B. Renard, C. Robert, and B. Gaubicher (2010), In situ balloon-borne measurements of HNO3 and HCl stratospheric vertical profiles influenced by polar stratospheric cloud formation during the 2005–2006 Arctic winter, *J. Geophys. Res.*, *115*, D21303, doi:10.1029/2009JD012947.

Hanisco, T. F., et al. (2002), Quantifying the rate of heterogeneous processing in the Arctic polar vortex with in situ observations of OH, *J. Geophys. Res.*, *107*(D20), 8278, doi:10.1029/2001JD000425.

Höpfner, M., et al. (2007), Validation of MIPAS $ClONO_2$ measurements, *Atmos. Chem. Phys.*, *7*, 257–281.

Jin, J. J., et al. (2006), Severe Arctic ozone loss in the winter 2004/2005: Observations from ACE-FTS, *Geophys. Res. Lett.*, *33*, L15801, doi:10.1029/2006GL026752.

Jones, A., G. Qin, K. Strong, K. A. Walker, C. A. McLinden, M. Toohey, T. Kerzenmacher, P. F. Bernath, and C. D. Boone (2011) A global inventory of stratospheric NO_y from ACE-FTS, *J. Geophys. Res.*, *116*, D17304, doi:10.1029/2010JD015465.

Joseph, J. K., W. J. Wiscombe, and J. A. Weinman (1976), The Delta-Eddington approximation for radiative flux transfer, *J. Atmos. Sci.*, *33*, 2452–2459.

Kawa, S. R., D. W. Fahey, L. E. Heidt, W. H. Pollock, S. Solomon, D. E. Anderson, M. Loewenstein, M. H. Proffitt, J. J. Margitan, and K. R. Chan (1992), Photochemical partitioning of the reactive nitrogen and chlorine reservoirs in the high-latitude stratosphere, *J. Geophys. Res.*, *97*(D8), 7905–7923, doi:10.1029/91JD02399.

Kerzenmacher, T., et al. (2008), Validation of NO_2 and NO from the Atmospheric Chemistry Experiment (ACE), *Atmos. Chem. Phys.*, *8*, 5801–5841.

Kondo, Y., U. Schmidt, T. Sugita, P. Aimedieu, M. Koike, H. Ziereis, and Y. Iwasaka (1994), Total reactive nitrogen, N_2O, and ozone in the winter Arctic stratosphere, *Geophys. Res. Lett.*, *21*(13), 1247–1250.

Lary, D. J., and J. A. Pyle (1991), Diffuse radiation, twilight and photochemistry, *J. Atmos. Chem.*, *13*, 373–392.

Li, J., and H. W. Barker (2005), A radiation algorithm with correlated-k distribution. Part I: Local thermal equilibrium, *J. Atmos. Sci.*, *62*, 286–309.

Manney, G. L., R. W. Zurek, A. O'Neill, and R. Swinbank (1994), On the motion of air through the stratospheric polar vortex, *J. Atmos. Sci.*, *51*, 2973–2994.

Manney, G. L., et al. (2007), Solar occultation satellite data and derived meteorological products: Sampling issues and comparisons with Aura Microwave Limb Sounder, *J. Geophys. Res.*, *112*, D24S50, doi:10.1029/2007JD008709.

Manney, G. L., et al. (2008), The high Arctic in extreme winters: Vortex, temperature, and MLS and ACE-FTS trace gas evolution, *Atmos. Chem. Phys.*, *8*, 505–522.

Manney, G. L., et al. (2009), Satellite observations and modeling of transport in the upper troposphere through the lower mesosphere during the 2006 major stratospheric sudden warming, *Atmos. Chem. Phys.*, *9*, 4775–4795.

McLinden, C. A., S. C. Olsen, B. Hannegan, O. Wild, M. J. Prather, and J. Sundet (2000), Stratospheric ozone in 3-D models: A simple chemistry and the cross-tropopause flux, *J. Geophys. Res.*, *105*(D11), 14,653–14,665, doi:10.1029/2000JD900124.

Mellqvist, J., B. Galle, T. Blumenstock, F. Hase, D. Yashcov, J. Notholt, B. Sen, J.-F. Blavier, G. C. Toon, and M. P. Chipperfield (2002), Ground-based FTIR observations of chlorine activation and ozone depletion inside the Arctic vortex during the winter of 1999/2000, *J. Geophys. Res.*, *107*(D20), 8263, doi:10.1029/2001JD001080.

Mengistu Tsidu, G., et al. (2005), NO_y from Michelson Interferometer for Passive Atmospheric Sounding on Environmental Satellite during the

Southern Hemisphere polar vortex split in September/October 2002, *J. Geophys. Res.*, *110*, D11301, doi:10.1029/2004JD005322.

Plummer, D. A., J. F. Scinocca, T. G. Shepherd, M. C. Reader, and A. I. Jonsson (2010), Quantifying the contributions to stratospheric ozone changes from ozone depleting substances and greenhouse gases, *Atmos. Chem. Phys.*, *10*, 8803–8820.

Polavarapu, S., S. Ren, Y. Rochon, D. Sankey, N. Ek, J. Koshyk, and D. Tarasick (2005), Data assimilation with the Canadian Middle Atmosphere Model, *Atmos. Ocean*, *43*(1), 77–100, doi:10.3137/ao.430105.

Pougatchev, N. S., B. J. Connor, and C. P. Rinsland (1995), Infrared measurements of the ozone vertical distribution above Kitt Peak, *J. Geophys. Res.*, *100*(D8), 16,689–16,697, doi:10.1029/95JD01296.

Randall, C. E., et al. (2005), Stratospheric effects of energetic particle precipitation in 2003–2004, *Geophys. Res. Lett.*, *32*, L05802, doi:10.1029/2004GL022003.

Randall, C. E., V. L. Harvey, C. S. Singleton, S. M. Bailey, P. F. Bernath, M. Codrescu, H. Nakajima, and J. M. Russell II (2007), Energetic particle precipitation effects on the Southern Hemisphere stratosphere in 1992–2005, *J. Geophys. Res.*, *112*, D08308, doi:10.1029/2006JD007696.

Randall, C. E., V. L. Harvey, D. E. Siskind, J. France, P. F. Bernath, C. D. Boone, and K. A. Walker (2009), NO_x descent in the Arctic middle atmosphere in early 2009, *Geophys. Res. Lett.*, *36*, L18811, doi:10.1029/2009GL039706.

Randel, W., M.-L. Chanin, and C. Michaut (2002), SPARC intercomparison of middle atmosphere climatologies, *WMO/TD 1142*, Geneva, Switzerland.

Ravishankara, A. R., J. S. Daniel, and R. W. Portmann (2009), Nitrous oxide (N_2O): The dominant ozone-depleting substance emitted in the 21st century, *Science*, *326*, 123–125.

Reinecker, M. M., et al. (2008), The GEOS-5 data assimilation system–Documentation of versions 5.0.1, 5.1.0, and 5.2.0, *NASA Tech. Memo., TM–2008–104606*, vol. 27, 118 pp.

Ren, S., S. Polavarapu, S. Beagley, Y. Nezlin, and Y. Rochon (2011) The impact of gravity wave drag on mesospheric anlayses of the 2006 stratospheric major warming, *J. Geophys. Res.*, *116*, D19116, doi:10.1029/2011JD015943.

Ridley, B. A., H. L. Son, D. R. Hastie, H. I. Schiff, J. C. McConnell, W. F. J. Evans, C. T. McElroy, J. B. Kerr, H. Fast, and R. S. O'Brien (1984), Stratospheric odd nitrogen: Measurements of HNO_3, NO, NO_2, and O_3 near 54°N in winter, *J. Geophys. Res.*, *89*(D3), 4797–4820, doi:10.1029/JD089iD03p04797.

Rodgers, C. D. (1976), Retrieval of atmospheric temperature and composition from remote measurements of thermal radiation, *Rev. Geophys.*, *14*(4), 609–624.

Rodgers, C. D. (1990), Characterization and error analysis of profiles retrieved from remote sounding measurements, *J. Geophys. Res.*, *95*(D5), 5587–5595, doi:10.1029/JD095iD05p05587.

Rodgers, C. D. (2000), Inverse Methods for Atmospheric Sounding: Theory and Practice, *Ser. Atmos. Oceanic Planet. Phys.*, vol. 2, 238 pp., World Sci., Singapore.

Rodgers, C. D., and B. J. Connor (2003), Intercomparison of remote sounding instruments, *J. Geophys. Res.*, *108*(D3), 4116, doi:10.1029/2002JD002299.

Rösevall, J. D., D. P. Murtagh, and J. Urban (2007), Ozone depletion in the 2006/2007 Arctic winter, *Geophys. Res. Lett.*, *34*, L21809, doi:10.1029/2007GL030620.

Rothman, L. S., et al. (2005), The HITRAN 2004 molecular spectroscopic database, *J. Quant. Spectrosc. Radiat. Transfer*, *96*, 139–204, doi:10.1016/j.jqsrt.2004.10.008.

Sander, S. P., M. Golden, M. J. Kurylo, C. E. Kolb, M. J. Molina, G. K. Moortgat, B. J. Finlayson-Pitts, and A. R. Ravishankara (2003), Chemical kinetics and photochemical data for use in atmospheric studies, *JPL Publ.*, *02–25*, 334 pp.

Santee, M. L., G. L. Manney, L. Froidevaux, W. G. Read, and J. W. Waters (1999), Six years of UARS Microwave Limb Sounder HNO_3 observations: Seasonal, interhemispheric, and interannual variations in the lower stratosphere, *J. Geophys. Res.*, *104*(D7), 8225–8246, doi:10.1029/1998JD100089.

Santee, M. L., I. A. MacKenzie, G. L. Manney, M. P. Chipperfield, P. F. Bernath, K. A. Walker, C. D. Boone, L. Froidevaux, N. J. Livesey, and J. W. Waters (2008), A study of stratospheric chlorine partitioning based on new satellite measurements and modeling, *J. Geophys. Res.*, *113*, D12307, doi:10.1029/2007JD009057.

Scinocca, J. F., N. A. McFarlane, M. Lazare, J. Li, and D. Plummer (2008), The CCCma third generation AGCM and its extension into the middle atmosphere, *Atmos. Chem. Phys.*, *8*, 7055–7074, doi:10.5194/acpd-8-7883-2008.

Solomon, P., B. Connor, J. Barrett, T. Mooney, A. Lee, and A. Parrish (2002), Measurements of stratospheric ClO over Antarctica in 1996–2000 and implications for ClO dimer chemistry, *Geophys. Res. Lett.*, *29*(15), 1708, doi:10.1029/2002GL015232.

Toon, G. C., J.-F. Blavier, B. Sen, R. J. Salawitch, G. B. Osterman, J. Notholt, M. Rex, C. T. McElroy, and J. M. Russell III (1999), Ground based observations of Arctic O_3 loss during spring and summer 1997, *J. Geophys. Res.*, *104*(D21), 26,497–26,510, doi:10.1029/1999JD900745.

Vigouroux, C., et al. (2008), Evaluation of tropospheric and stratospheric ozone trends over Western Europe from ground-based FTIR network observations, *Atmos. Chem. Phys.*, *8*, 6865–6886, doi:10.5194/acp-8-6865-2008.

Viscardy, S., Q. Errera, Y. Christophe, S. Chabrillat, and J.-C. Lambert (2010), Evaluation of ozone analyses from UARS MLS assimilation by BASCOE between 1992 and 1997, *IEEE J. Sel. Top. Appl. Earth Obs. Remote Sens.*, *3*(2), 190–202, doi:10.1109/JSTARS.2010.2040463.

Wolff, M. A., et al. (2008), Validation of HNO_3, $ClONO_2$, and N_2O_5 from the Atmospheric Chemistry Experiment Fourier Transform Spectrometer (ACE-FTS), *Atmos. Chem. Phys.*, *8*, 3529–3562, doi:10.5194/acp-8-3529-2008.

Wood, S. W., R. L. Batchelor, A. Goldman, C. P. Rinsland, B. J. Connor, F. J. Murcray, T. M. Stephen, and D. N. Heuff (2004), Ground-based nitric acid measurements at Arrival Heights, Antarctica, using solar and lunar Fourier transform infrared observation, *J. Geophys. Res.*, *109*, D18307, doi:10.1029/2004JD004665.

World Meteorological Organization (WMO) (2007 Scientific assessment of ozone depletion: 2006, *WMO Global Ozone Res. Monit. Proj. Rep. 50*, Geneva, Switzerland.

World Meteorological Organization (WMO) (2011), Scientific assessment of ozone depletion: 2010, *WMO Global Ozone Res. Monit. Proj. Rep. 52*, Geneva, Switzerland.

R. L. Batchelor, Atmospheric Chemistry Division, National Center for Atmospheric Research, 3450 Mitchell Ln., Boulder, CO 80310, USA.

P. F. Bernath, Department of Chemistry, University of York, Heslington, York YO10 5DD, UK.

S. Chabrillat, Chemical Weather Services, Belgian Institute for Space Aeronomy, 3 Ave. Circulaire, B-1180 Brussels, Belgium.

M. P. Chipperfield and W. Feng, Institute for Climate and Atmospheric Science, School of Earth and Environment, University of Leeds, Leeds LS2 9JT, UK.

W. H. Daffer and G. L. Manney, Jet Propulsion Laboratory, 4800 Oak Grove Dr., Pasadena, CA 91109, USA.

J. R. Drummond, Department of Physics and Atmospheric Science, Dalhousie University, 6310 Coburg Rd., Halifax, NS B3H 1Z9, Canada.

A. I. Jonsson, F. Kolonjari, R. Lindenmaier, K. Strong, and K. A. Walker, Department of Physics, University of Toronto, 60 St. George St., Toronto, ON M5S 1A7, Canada. (rodica@atmosp.physics.utoronto.ca)

C. McLinden, Air Quality Research Division, Environment Canada, 4905 Dufferin St., Downsview, ON M3H 5T4, Canada.

R. Ménard, Air Quality Research Division, Environment Canada, 2121 Transcanada Hwy., Dorval, QC H9P 1J3, Canada.